On the Oxygen Nonstoichiometry in Thermoelectric Oxides

Matthias Schrade

Dissertation for the degree of Philosophiae Doctor

Department of Physics
Faculty of Mathematics and Natural Sciences

University of Oslo

March 2014

© Matthias Schrade, 2014

Series of dissertations submitted to the
Faculty of Mathematics and Natural Sciences, University of Oslo
No. 1516

ISSN 1501-7710

All rights reserved. No part of this publication may be
reproduced or transmitted, in any form or by any means, without permission.

Cover: Inger Sandved Anfinsen.
Printed in Norway: AIT Oslo AS.

Produced in co-operation with Akademika Publishing.
The thesis is produced by Akademika Publishing merely in connection with the thesis defence. Kindly direct all inquiries regarding the thesis to the copyright holder or the unit which grants the doctorate.

Summary

The interest in thermoelectric oxides as candidate materials for high temperature waste heat recovery has generated vital scientific activity during the last years. However, while it is well established in several other fields of materials science that the electronic structure of oxides at high temperatures can be significantly modified by the formation of oxygen vacancies, the precise control of the sample and its surrounding atmosphere is rather seldomly seen in scientific publications on high temperature thermoelectric oxides. Therefore, during this thesis, I have investigated the influence of the oxygen content on the properties of two of the most prominent thermoelectric oxides.

A variation of the oxygen content of a material at high temperatures can be achieved by a variation of the surrounding atmosphere and the subsequent in- and out-diffusion of oxygen ions until the new thermodynamic equilibrium state is reached. Oxygen vacancies can usually be described as effectively charged point defects and the precise control of their concentration provides a means to change the charge carrier concentration of a material *in situ*.

Therefore, one goal of this thesis is to establish that the high temperature thermoelectric characterisation of oxides should preferably be done under controlled atmospheric conditions. In fact, part of the scatter observed in published results on nominally identical samples can be explained by (unintentionally) different oxygen content, due to different measurement atmospheres or sample kinetics. Moreover, the results from this thesis aim to contribute to the fundamental understanding of the charge transport processes in the studied and related materials.

The thesis comprises the design and characterisation of an appropriate system to measure the electrical transport properties of the materials under investigation (Manuscript 3). Manuscript 1 and 4 study one of the most prominent thermoelectric oxides: Misfit calcium cobalt oxide $(Ca_2CoO_{3-\delta})_q(CoO_2)$ (CCO), which shows one of the best reproducible p-type thermoelectric performances among all oxides.

In Manuscript 1, we established a defect chemical model of this material. Due to its misfit structure, it is inherently mixed-valent, so that a modified defect notation was chosen. The dependency of both electrical conductivity and Seebeck coefficient on the oxygen content was measured in a wide range of temperature and oxygen partial pressure. It was concluded that – at high temperatures – charge carriers should be

described as itinerant in this material. We further showed that the often used Heikes formula cannot be used for a quantitative analysis of the Seebeck coeffcient in CCO. Instead, we suggested a modified Mott formula with a significant contribution from the energy dependent mobility to describe the Seebeck coefficient in CCO.

In Manuscript 4, a combined experimental and theoretical study of the oxygen nonstoichiometry in CCO is presented. Based on DFT-calculations and experimental Raman-spectroscopy, it is shown that oxygen is preferentially removed from an atomic position within the central layer of the Ca_2CoO_3-subsystem. The computational results further indicated that the electronic properties are sensitive to small variations in the crystal structure. The thermodynamics of oxidation were investigated by three different techniques (TG, TG-DSC, and DFT) and differences were discussed.

In Manuscript 2, the high temperature charge transport in $CaMnO_{3-\delta}$ (CMO) was investigated. CMO is – when doped with small amounts of niobium – among the most promising n-type oxides with a figure of merit reaching 0.3 at high temperatures. When forming oxygen vacancies – thereby increasing the electron concentration of the material – we observed an unusual simultaneous decrease of both conductivity and the absolute value of the Seebeck coefficient. These findings were analysed as an indication of strongly interacting small polarons as the charge carrier in this material. We generalised this result to develop a simple model for the powerfactor and concluded that mutual Coulomb repulsion limits the thermoelectric performance of these materials.

Acknowledgement

This work was carried out within the project "Thermoelectric Oxides for High Temperature Waste Heat Recovery" (THERMEL), funded by the RENERGI programme of the Norwegian Research Council.

Firstly, I would like to thank my supervisors, Terje Finstad and Truls Norby, for allowing me to work independently and develop my own ideas, but providing interest, advice, and guidance, whenever I got lost on the way.

I am also grateful for the privilege to work in the social, helpful, and inspiring environment of the FASE group. Thanks to all previous and present members for making this a nice place to work and – of course – for uncounted coffee breaks, foosball matches, and social gatherings.

Especially, I thank Harald Fjeld, for being a great office mate, patient teacher of (defect) chemistry, and omniscient lab-encyclopedia. It is safe to say that this thesis would have looked different without you!

A big thank you also to our cohabitants from the structural physics group, especially Ole-Bjørn Karlsen and Kjetil Valset, for providing practical assistance and help. Simone Casolo deserves my deep respect for patiently enduring my endless questions around his DFT results.

My stay in the group of Sean Li in Sydney was pleasant, interesting, and scientifically productive. I'd like to thank all the people I met there, who helped making me feel at home at the other side of the world within only three months.

I am also happy to have met Leyre Sagarna and Christophe Heinrich on conferences, sharing the experience and struggles of being a PhD-student and resulting in mini-collaborations.

Further, I am deeply indebted to my parents and family for almost three decades of unconditional support and advice. Finally, I thank my friends and especially Tina for simply being there.

Oslo, March 2014

Matthias Schrade

Contents

1 Introduction

In recent years, the imperative need to develop better, more efficient, and environmentally friendly energy technologies has pushed forward the research on functional materials in several different fields. For example, a significant part of the energy from many industrial processes is lost as waste heat and the upconversion into usable, less entropic forms of energy could be a promising way of increasing the efficiency of these processes. Heat engines like the Stirling engine may be the method of choice in large-scale, stationary applications, while generators based on thermoelectric materials offer an elegant way to re-use part of the waste heat in small, decentralised applications, as for example in cars.

A thermoelectric generator is built up of many couples of p- and n-type conducting legs, connected electrically in series and thermally in parallel. When a temperature difference is present across the module, each leg will generate a (usually small) voltage due to the Seebeck effect. This voltage (or better: the sum of the voltages of all legs coupled in series) can then be used to drive a current through a load resistance. The main requirements of a good thermoelectric material are thus intuitively clear: (i) high Seebeck coefficient to generate a high open-circuit voltage (ii) low electrical resistivity to obtain a high output power at the load resistance (iii) low thermal conductivity to minimise the heat flow between the warm and the cold side.

More precisely, one can show [1] that the efficiency η of a thermoelectric generator is

$$\eta = \frac{T_{\mathrm{Hot}} - T_{\mathrm{Cold}}}{T_{\mathrm{Hot}}} \cdot \frac{\sqrt{1 + ZT_{\mathrm{av}}} - 1}{\sqrt{1 + ZT_{\mathrm{av}}} + T_{\mathrm{Cold}}/T_{\mathrm{Hot}}} \tag{1.1}$$

where T_{Hot}, T_{Cold}, and T_{av} are, respectively, the hot side, cold side and average temperature, and Z is the effective figure of merit of the p-n-couple, defined as:

$$Z = \frac{(\alpha_{\mathrm{p}} - \alpha_{\mathrm{n}})^2}{\left(\sqrt{\kappa_{\mathrm{p}}\rho_{\mathrm{p}}} + \sqrt{\kappa_{\mathrm{n}}\rho_{\mathrm{n}}}\right)^2}, \tag{1.2}$$

Here, α is the Seebeck coefficient, ρ the electrical resistivity, and κ the thermal conductivity. The index n (or p) indicates the n-type (or p-type) leg. The effective figure of merit Z is usually close to the average of the individual figures of merit z of the p- and n-materials. Thus, the by far most reported number in thermoelectric

research is the single material property zT:[1]

$$zT = \frac{\alpha^2 \sigma}{\kappa} T \tag{1.3}$$

where $\sigma = 1/\rho$ is the electrical conductivity. Today, thermoelectric power generation is mostly used in niche applications, where size, reliability and silent operation are more important than the conversion efficiency. State-of-the-art thermoelectric materials are, for example, Bi_2Te_3 for low temperature applications ($zT(300\,\mathrm{K}) \approx 1.0$), alloys og Ag_2SbTe_2 and GeTe ("TAGS") ($zT_{\mathrm{Max}} \approx 1.2$ around 800 K), and SiGe-alloys for high temperature applications ($zT \approx 0.8$ for $T \geq 1000\,\mathrm{K}$) (For a more extensive review on conventional thermoelectric materials, see e.g. [2] and references therein). The potential impact of thermoelectric materials has been disputed [3], but it is clear that the zT of many studied materials needs to be improved to become a competitive alternative in commercial applications. Furthermore, questions of module design, scalability, price, and long-term stability need to be addressed in order to fully evaluate the potential impact of thermoelectrics.

Oxides have been investigated as potential candidate materials for many different applications, including - among others - superconductors, magnetic storage devices, photovoltaics, ionic conductors, and piezoelectric devices, and their functionality is often found to be comparable or even superior to other, non-oxide materials. This is most impressively illustrated by the discovery of the high temperature superconductors found in the layered cuprate family.

However, in the context of thermoelectrics, oxides have widely been neglected due to their strong ionic bonding, resulting in low carrier mobilities, and thereby contradicting predictions for optimal thermoelectric performance made from the conventional thermoelectric theory. But in 1997, Terasaki *et al.* found the combination of low, metallic resistivity with a large Seebeck coefficient in Na_xCoO_2 [4]. The charge carrier concentration for this material is more than one order of magnitude higher than predicted for optimal thermoelectric performance from conventional transport theory and as realised in other, established thermoelectric materials. These findings have led to a continuously increasing research activity on thermoelectric oxides as candidate materials for high temperature waste heat recovery.

Compared to conventional thermoelectric materials based on heavy p-block elements like Te, Sb and Pb, oxides have several appealing advantages: (i) They are stable in air up to high temperatures, increasing the potential temperature application range and simplifying the module design and fabrication. (ii) They consist of cheap, non-toxic and abundant elements, making an industrial scale-up possible.

The vast majority of the publications on thermoelectric oxides either investigates

[1] One includes the factor T to obtain a dimensionless figure

the fundamental properties at temperatures below 300 K or studies the thermoelectric properties of a material doped with different elements at high temperatures, often depending on whether the authors have a background in physics or materials science/chemistry. This results in an often inconsistent and incomplete understanding of the charge transport processes at high temperatures.

In addition, as nearly unlimited combinations of different oxide structures, dopants, and processing technologies can be studied, the trial-and-error approach is neither economically nor temporally efficient in finding the best thermoelectric oxide and to assess the potential applicability of these materials in energy harvesting applications.

In this thesis, I have therefore studied the high temperature properties of two of the best known thermoelectric oxides – $(Ca_2CoO_3)_q(CoO_2)$ as a p-type and $CaMnO_3$ as an n-type material – in detail. By precisely controlling the surrounding atmosphere, it is possible to control the concentration of oxygen vacancies and to investigate their influence on the thermoelectric properties. Firstly, this demonstrates the influence of the experimental conditions on the measured thermoelectric performance. Experiments performed on identical samples can result in significantly different results when measured under different conditions, possibly leading to confusion when evaluating the thermoelectric performance. On the other hand, the control of the concentration of oxygen vacancies of the sample provides a means to vary the charge carrier concentration within a significant range *in situ*, thereby allowing to test, reject, and propose models to understand the charge transport in these materials.

The introductory part presents the theoretical background for the physical parameters studied, as well as the defect chemical concept used within this thesis (Chapter 2 and 3). In Chapter 4, the most prominent thermoelectric oxides are presented and the motivation for choosing the materials studied in this thesis are explained. Some additional details of the experimental techniques, not included in the different manuscripts, are presented in Chapter 5. After the most central findings are presented in the form of scientific papers (Chapter 6), the results will be summarised and discussed as a whole in Chapter 7.

2 Thermoelectric Transport

In the following chapter, we present a short introduction to the theoretical description of transport parameters within Boltzmann's transport theory. In particular, a motivation of several formulae for the electrical conductivity and the Seebeck coefficient, which are frequently found in the literature, will be given. The detailed knowledge of approximations made during derivation is important, when chosing the right model to describe the properties of a certain material.

2.1 Thermodynamic Considerations

Before we address the electrical transport properties of a solid, we shortly want to line out a description of the thermoelectric effects as seen from an *irreversible thermodynamics* perspective, following [5, 6].

This approach offers an intuitive understanding of the physical meaning of α as the "entropy per transported charge carrier", which is later used to derive Heikes' formula.

Thermoelectric phenomena like the Seebeck, the Peltier, and the Thomson effect generally relate the flows of heat and current. The different effects are mutually linked via the Kelvin relations.

The Peltier coefficient Π is defined as the heat Q, which is reversibly evolved at a junction between two materials, per unit current flowing accross, when no temperature gradient is present.

$$\Pi = \frac{Q_{\mathrm{rev}}}{qJ_{\mathrm{N}}} \tag{2.1}$$

q is the charge per carrier and J_{N} the particle flow. In addition, irreversible heat will evolve due to standard Joule heating quadratic in J_{N}, which we can neglect when the particles are moved sufficiently slowly. This condition of slowness already suggests some kind of equilibrium process, which is thermodynamically reversible. Thus, we can express the evolved heat Q_{rev} in terms of an entropy flow J_{S}:

$$Q_{\mathrm{rev}} = T \cdot J_{\mathrm{S}} \tag{2.2}$$

Using one of the fundamental Kelvin relations $\Pi = T\alpha$, relating the Peltier and

Seebeck effect, we obtain

$$\alpha = \frac{J_\mathrm{S}}{qJ_\mathrm{N}} \tag{2.3}$$

We can see from Eq. (2.3), that the Seebeck coefficient α can be thought of as the entropy transported by a carrier divided by its charge.

2.2 Boltzmann Transport Theory

The outline of this section generally follows the book of Goldsmid [1], with additional contributions taken from the books by Wilson and Ziman [7,8]. In solids, the quantum mechanical description of electrons at equilibrium is goverened by the Fermi-Dirac distribution, stating that a state at energy E is occupied with a propability of

$$f_0(E) = \frac{1}{\exp\left(\frac{E-E_\mathrm{F}}{\mathrm{k_B}T}\right)+1} \tag{2.4}$$

where E_F is the Fermi energy and T is the absolute temperature. By external fields - e.g. an electrical field or a temperature gradient - the systems can be disturbed out from its equilibrium state f_0 and we denote the new distribution function by f. Scattering events will drive the sytem back to equilibrium. Under steady-state conditions, those two effects will balance out:

$$0 = \left.\frac{\mathrm{d}f}{\mathrm{d}t}\right|_\mathrm{fields} + \left.\frac{\mathrm{d}f}{\mathrm{d}t}\right|_\mathrm{scattering} \tag{2.5}$$

A common simplification of Eq. (2.5) is the *relaxation time approximation* for the scattering term, stating that a system perturbed from its equilibrium state f_0 will relax back to f_0 exponentially, with a characteristic time τ:

$$\left.\frac{\mathrm{d}f}{\mathrm{d}t}\right|_\mathrm{scattering} = -\frac{f(E)-f_0(E)}{\tau(E)} \tag{2.6}$$

Here, τ is the average scattering time for an electron of energy E. It is further often assumed that τ can be expressed as $\tau_0 E^r$, with the exponent r being dependent on the scattering process.

By using Liouville's theorem on the invariance of volume occupied in phase space, as long scattering is neglected, the fields term in Eq. (2.5) can be written as

$$\frac{f(E)-f_0(E)}{\tau} = -\dot{k}\nabla_k f(E) - \dot{r}\nabla_r f(E) \tag{2.7}$$

Equation (2.7) can be simplified further by assuming steady state ($\dot{k}=0$) and that

the system is not far from its equilibrium state ($\frac{\mathrm{d}f_0}{\mathrm{d}E} \approx \frac{\mathrm{d}f}{\mathrm{d}E}$):

$$\frac{f(E) - f_0(E)}{\tau} = u \frac{\partial f_0(E)}{\partial E} \left[\frac{\partial E_\mathrm{F}}{\partial x} + \frac{E - E_\mathrm{F}}{T} \cdot \frac{\partial T}{\partial x} \right] \tag{2.8}$$

where $u = \dot{r}$ is the electron velocity in the direction of the temperature gradient. In general, the electric current density i and the heat current density j can be written as[1]

$$i = \mp \int_0^\infty e\, u f(E) D(E)\, \mathrm{d}E \tag{2.9}$$

$$j = \int_0^\infty u(E - E_\mathrm{F})\, f(E)\, D(E)\, \mathrm{d}E \tag{2.10}$$

where $(E - E_\mathrm{F})$ is the amount of heat (or energy) transported by each carrier and $D(E)$ is the density of states of energy E. The upper and lower signs correspond to electrons and holes, respectively. By replacing f with $f - f_0$ – since there is no flux of heat or current in equilibrium – and approximating the carrier velocity u along x by one third of its total thermal kinetic energy $2E/3m^*$, we can rewrite Eqs. (2.9) and (2.10) as:

$$i = \mp \frac{2e}{3m^*} \int_0^\infty D(E)\tau(E)E \cdot \frac{\partial f_0(E)}{\partial E} \left[\frac{\partial E_\mathrm{F}}{\partial x} + \frac{E - E_\mathrm{F}}{T} \cdot \frac{\partial T}{\partial x} \right] \mathrm{d}E \tag{2.11}$$

$$j = \pm \frac{E_\mathrm{F}}{e} i + \frac{2}{3m^*} \int_0^\infty D(E)\tau(E)E^2 \cdot \frac{\partial f_0(E)}{\partial E} \left[\frac{\partial E_\mathrm{F}}{\partial x} + \frac{E - E_\mathrm{F}}{T} \cdot \frac{\partial T}{\partial x} \right] \mathrm{d}E \tag{2.12}$$

The different transport coefficients can then be obtained by employing the relevant boundary conditions to Eqs. (2.11) and (2.12). For example, the electrical conductivity is given as the ratio of the electrical current i and the electrical field E ($\mathrm{d}E_\mathrm{F}/\mathrm{d}x = eE$) when $\mathrm{d}T/\mathrm{d}x = 0$. One obtains:

$$\sigma = \mp \frac{2e^2}{3m^*} \int_0^\infty D(E)\tau(E)E \frac{\mathrm{d}f_0(E)}{\mathrm{d}E} \mathrm{d}E \tag{2.13}$$

The Seebeck coefficient is the ratio of the electric field and the temperature gradient $\mathrm{d}T/\mathrm{d}x$ under the boundary condition $i = 0$:

$$\alpha = \pm \frac{1}{eT} \left[E_F - \frac{\int_0^\infty D(E)\tau(E)E^2 \frac{\mathrm{d}f_0}{\mathrm{d}E} \mathrm{d}E}{\int_0^\infty D(E)\tau(E)E \frac{\mathrm{d}f_0}{\mathrm{d}E} \mathrm{d}E} \right] \tag{2.14}$$

The thermal conductivity is the ratio of the heat current j and the temperature field

[1] Note that the definition of the heat flux considers only the heat transported by the electrons. Additional contributions from phonons or interaction between phonons and electrons - for example the *phonon drag effect* - are not included.

$-\mathrm{d}T/\mathrm{d}x$ under the same condition ($i = 0$):

$$\kappa_\mathrm{e} = \frac{2}{3m^*T}\left[\frac{\left\{\int_0^\infty D(E)\tau(E)E^2\frac{\mathrm{d}f_0}{\mathrm{d}E}\mathrm{d}E\right\}^2}{\int_0^\infty D(E)\tau(E)E\frac{\mathrm{d}f_0}{\mathrm{d}E}\mathrm{d}E} - \int_0^\infty D(E)\tau(E)E^3\frac{\mathrm{d}f_0}{\mathrm{d}E}\mathrm{d}E\right] \tag{2.15}$$

Using the definition

$$K_\mathrm{s} = -\frac{2T}{3m^*}\cdot\int_0^\infty D(E)\tau(E)E^{s+1}\frac{\mathrm{d}f_0}{\mathrm{d}E}\mathrm{d}E \tag{2.16}$$

the transport coefficients can be written in a compact form:

$$\sigma = \frac{e^2}{T}K_0 \tag{2.17}$$

$$\alpha = \pm\frac{1}{eT}\left(E_\mathrm{F} - \frac{K_1}{K_0}\right) \tag{2.18}$$

$$\kappa_\mathrm{e} = \frac{1}{T^2}\left(K_2 - \frac{K_1^2}{K_0}\right) \tag{2.19}$$

By inserting $\tau(E) = \tau_0 E^r$ and the parabolic band expression for the density of states ($D(E) \propto \sqrt{E}$), the integrals K_s can be eventually related to the Fermi-Dirac integrals F_n:

$$K_\mathrm{s} = \frac{8\pi}{3}\left(\frac{2}{h^2}\right)^{3/2}\sqrt{m^*}T\tau_0(s+r+3/2)(\mathrm{k_B}T)^{s+r+3/2}F_{s+r+1/2} \tag{2.20}$$

with

$$F_\mathrm{n}(\eta) = \int_0^\infty \xi^n f_0(\xi)\mathrm{d}\xi \tag{2.21}$$

where $\xi = E/\mathrm{k_B}T$ is the reduced energy. The different F_n can be solved numerically for different values of η. For the two limiting cases of a metal ($\eta \gg 1$) and a non-degenerate semicondutor ($\eta \ll 1$), the integrals can be solved analytically, leading to relatively simple expressions for the transport coefficients.

2.2.1 Metals

We consider the degenerate case of a metal first. $F_\mathrm{n}(\eta)$ can be expanded into a power series (for the mathematical details, see e.g. the book by Mott and Jones [9]):

$$F_\mathrm{n}(\eta) = \frac{\eta^{n+1}}{n+1} + n\eta^{n-1}\frac{\pi^2}{6} + \ldots \tag{2.22}$$

By combining Eqs. (2.17), (2.20) and the first term in (2.22), one obtains for the conductivity:

$$\sigma = \frac{8\pi}{3}\left(\frac{2}{h^2}\right)^{3/2}e^2\sqrt{m^*}\tau_0 E_\mathrm{F}^{r+3/2} \tag{2.23}$$

To get a non-vanishing expression for the thermal conductivity, the first two terms in Eq. (2.22) have to be considered. One eventually arrives at

$$\frac{\kappa_\mathrm{e}}{\sigma} = \underbrace{\frac{\pi^2}{3}\left(\frac{\mathrm{k_B}}{e}\right)^2}_{=:L} \cdot T \tag{2.24}$$

which is the Wiedemann-Franz law with the Lorenz number $L = 2.44 \cdot 10^{-8}\,\mathrm{W\Omega K^{-2}}$. In the general case, the ratio L between κ_e and σT can be calculated from Eqs. (2.17) and (2.19) to:

$$L = \left(\frac{\mathrm{k_B}}{e}\right)^2 \cdot \frac{3F_0F_2 - 4F_1^2}{F_0^2} \tag{2.25}$$

where we chose $r = -1/2$, assuming acoustic phonon scattering. The Seebeck coefficient can be calculated to

$$\alpha = \mp\frac{\pi^2}{3}\,\frac{\mathrm{k_B}}{e}\,\frac{r+3/2}{\eta} \tag{2.26}$$

Combining Eqs. (2.23) and (2.26), one gets

$$\alpha = \frac{\pi^2}{3}\,\frac{\mathrm{k_B^2}}{e}\,T\,\left.\frac{\mathrm{d}\ln\sigma(E)}{\mathrm{d}E}\right|_{E=E_\mathrm{F}} \tag{2.27}$$

which is commonly referred to as the *Mott formula*. By inserting $\sigma = n(E)e\mu(E)$, one arrives at

$$\alpha = \frac{\pi^2}{3}\,\frac{\mathrm{k_B^2}}{e}\,T\left[\frac{D(E)}{n} + \frac{\mathrm{d}\ln\mu(E)}{\mathrm{d}E}\right]_{E=E_\mathrm{F}} \tag{2.28}$$

The first term can be identified with the specific heat per electron C_e/n. We make use of Eq. (2.28) in Manuscript 1 and justify the metallic treatment of $(Ca_2CoO_3)_q(CoO_2)$ in section 3.2. By using an alternative expression of the conductivity, $\sigma = D(E)\,v^2\,\tau$ [6, 7], one gets

$$\alpha = \frac{\pi^2}{3}\,\frac{\mathrm{k_B^2}}{e}\,T\left(\frac{\mathrm{d}\ln D(E)}{\mathrm{d}E} + \frac{\mathrm{d}\ln v^2(E)}{\mathrm{d}E} + \frac{\mathrm{d}\ln\tau(E)}{\mathrm{d}E}\right)_{E=E_\mathrm{F}} \tag{2.29}$$

which can be rewritten as[2]

$$\alpha = \frac{\pi^2}{3}\,\frac{\mathrm{k_B^2}}{eE_\mathrm{F}}\,T\left(\frac{\mathrm{d}\ln D(E)}{\mathrm{d}\ln E} + \frac{\mathrm{d}\ln v^2(E)}{\mathrm{d}\ln E} + \frac{\mathrm{d}\ln\tau(E)}{\mathrm{d}\ln E}\right)_{E=E_\mathrm{F}} \tag{2.30}$$

v is an average velocity of the charge carrier. For free electrons, one has $D(E) \propto \sqrt{E}$, $v(E) \propto \sqrt{E}$, and $E_\mathrm{F} = h^2/8m \cdot (3n/\pi)^{2/3}$. Further, assuming acoustic phonon scattering ($\tau \propto E^{-1/2}$), one finally gets a relationship between the Seebeck coefficient

[2] Assuming functional dependencies of $\tau(E)$, $D(E)$, and $v(E)$ in the form of E^x

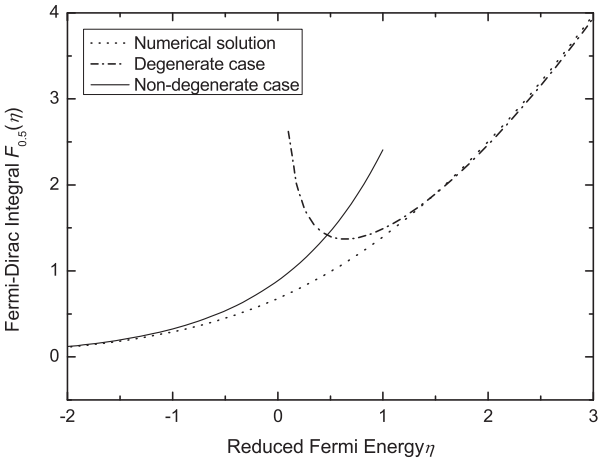

Figure 2.1: The approximations for the Fermi-Dirac integrals F_n compared to the numerical solution, calculated using Wolfram Mathematica 6. $n = 1/2$ is shown as an example. The degenerate approximation $\eta \gg 1$ (Eq. (2.22)) yields good results for $\eta > 2$, while the non-degenerate case (Eq. (2.32)) gives an acceptable agreement for $\eta < -1$.

and the carrier concentration n valid for metals or degenerate semiconductors [2,10]:

$$\alpha = \frac{8\pi^2 \mathrm{k}_\mathrm{B}^2}{3eh^2} m^* T \left(\frac{\pi}{3n}\right)^{2/3} \tag{2.31}$$

2.2.2 Semiconductors

The other analytical expression for the transport integrals can be derived for the case $\eta \ll 1$, i.e. where the Fermi level lies deep inside a band gap, as is the case for a non-degenerate semiconductor. In this case, one can approximate the Fermi-Dirac integrals with a Maxwellian distribution:

$$F_\mathrm{n} \approx \int_0^\infty \xi^n \exp \eta - \xi \, \mathrm{d}\xi = e^\eta \cdot \Gamma(n+1) \tag{2.32}$$

Here, we introduced the Γ-function

$$\Gamma(x) = \int_0^\infty a^{x-1} \exp -a \, \mathrm{d}a \tag{2.33}$$

Integration by parts yields $\Gamma(n+1) = n\Gamma(n)$. For a non-degenerate semiconductor, the integral K_s can thus be written as

$$K_\mathrm{s} = \frac{8\pi}{3} \left(\frac{2}{h^2}\right)^{3/2} \sqrt{m^*}\, T \tau_0 \, (\mathrm{k}_\mathrm{B} T)^{s+r+3/2} \, \Gamma(s+r+1/2) \exp \eta \tag{2.34}$$

The transport coefficients are then

$$\sigma = \frac{8\pi}{3}\left(\frac{2}{h^2}\right)^{3/2}\sqrt{m^*}\,e^2\tau_0\,(\mathrm{k_B}T)^{r+3/2}\,\Gamma(r+1/2)\exp\eta \tag{2.35}$$

$$\alpha = \mp\frac{\mathrm{k_B}}{e}\left[\eta - (r+5/2)\right] \tag{2.36}$$

$$L = \frac{\kappa_\mathrm{e}}{\sigma T} = \left(\frac{\mathrm{k_B}}{e}\right)^2 \cdot (r+5/2) \tag{2.37}$$

Substituting the standard expression for the carrier concentration n in a semiconductor in Eq. (2.36)

$$n = 2\left(\frac{m^*\mathrm{k_B}T}{2\pi\hbar^2}\right)^{3/2}\exp -\eta = N_0\,\exp -\eta \tag{2.38}$$

we get an often used relation between the Seebeck coefficient and the carrier concentration in a semiconductor:

$$\alpha = \mp\frac{\mathrm{k_B}}{e}\left(\ln\frac{N_0}{n} - (5/2+r)\right) \tag{2.39}$$

N_0 is the effective density of states of valence and conduction band, respectively. The comparison between the numerical solution of $F_{1/2}$ and the two limiting cases (2.22) and (2.32) is shown in Fig. 2.1. The numerical solutions of the Fermi-Dirac-integrals also allow it to calculate the transport coefficients, assuming a dominating scattering parameter r: The conductivity (Eq. (2.17)), the Seebeck coefficient (Eq. (2.18)), and the numerator $\alpha^2\sigma$ of the figure of merit (= the power factor) are shown in Fig. 2.2. The highest power factor is obtained for $\eta \approx 0$, i.e. where the Fermi-level lies close to a band edge. Unfortunately, optimal thermoelectric performance is thus expected in a region where the simplified analytical expressions for the transport coefficients describe the numerical solution only poorly.

2.2.3 Transport via Localised States

So far, we reviewed electronic transport in idealised solids, where the charge carriers move itinerantly within bands, and are scattered back to an equilibrium state within a characteristic scattering time τ. In polar solids (i.e. materials with a significant ionic character of the bond), charge carriers will interact with and deform the lattice in their surrounding. When moving through the crystal, this deformation follows the carrier and the entity of lattice deformation and charge carrier can be treated as a quasi-particle, named polaron. Depending on the strength of the electron-phonon interaction, different cases can be distinguished. When the interaction is relatively weak, the associated lattice deformation is spread over a significant volume in the

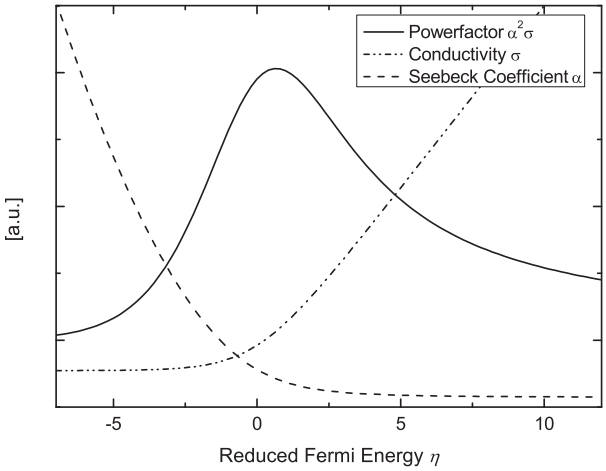

Figure 2.2: Schematic of the conductivity σ, the Seebeck coefficient α, and the power factor $\alpha^2\sigma$ calculated for $r = -1/2$. Note that the power factor is maximal in a region for η where the analytical approximations do not describe the numerical solution (c.f. Fig. 2.1).

crystal. Theoretical treatment of such a *large* polaron is similar to that of a regular band electron with an increased effective mass m^*. On the other hand, when the electron-phonon coupling is strong, the carrier may be trapped in the potential well caused by the deformation of the lattice around it. The electronic transport then occurs via thermally activated hopping processes between localised states. The mobility can be expressed as

$$\mu(T) = \frac{\mu_0}{T} \exp\left(-\frac{E_\mathrm{a}}{\mathrm{k_B}T}\right) \tag{2.40}$$

An expression for the Seebeck coefficient for a hopping conductor is easiest to derive from Eq. (2.3), stating that α is a measure for the entropy per charge carrier. At high temperatures, but with strong on-site repulsion U ($\mathrm{k_B} \ll U$), all possible configurations have the same energy and are thus equally likely to be realised at a given moment. The parameter U scales the electron-electron interaction term in the Hamiltonian of the Hubbard model [11].

The entropy of such system is calculated by the classical Boltzmann formula

$$S = -\mathrm{k}_B \ln \Omega \tag{2.41}$$

where Ω is the number of possible states. Accordingly, we get for the Seebeck coeffi-

cient

$$\alpha = -\frac{k_B}{e} \frac{\partial \ln \Omega(x)}{\partial x} \tag{2.42}$$

Considering a system of N sites filled with n electrons, Ω can be calculated and one obtains the famous Heikes formula:

$$\alpha = -\frac{k_B}{e} \cdot \ln\left(\frac{1-c}{c}\right) \tag{2.43}$$

where $c = n/N$.

Polaronic effects are common in oxides due to the dominating ionic character of the bonds due to the high electronegativity of oxygen. This will be discussed in detail in Manuscripts 1 and 2. One should further note that many transition metal oxides show deviations from the non-interacting electron gas approximation used to derive the general expressions for the transport coefficients Eqs. (2.17)-(2.19). These effects are summarised under the term *electronic correlation*. Consequences of correlated charge carriers on the transport properties are difficult to treat theoretically and are discussed in the literature (for a theoretical overview, see e.g. Ref. [12]). Considerable effort has been devoted to develop a theory to include correlation effects into standard DFT calculations, which usually results in the introduction of an empirical parameter U to mimic the mutual repulsion of charge carriers [13, 14].

3 Oxygen Defects in Oxides

In this chapter, some fundamental descriptions of the defect structure of an oxide material are given and the influence of oxygen nonstoichiometry on the electronic properties is discussed. When effectively charged defects are formed in a material, the concentration of other charged species, as for example mobile electrons or holes, will change to keep the overall charge in balance. A central part of this thesis is to investigate *how* the electric transport coefficients α and σ vary when the carrier concentration changes and trying to relate this behaviour with different models for the electronic transport developed in the previous section.

Primarily, we make use of the Kröger-Vink-notation[1] to describe point defects, but we include a section about its analogy to a band-picture description of the electronic properties. As a relatively simple example, we chose an acceptor-doped perovskite $AB_{1-x}C_xO_3$, such as acceptor-doped $SrTiO_3$. The electronic properties are well described by a non-degenerate semiconductor, where analytical expressions of the general integrals Eqs. (2.17)-(2.19) exist.

3.1 Oxygen Nonstoichiometry and its Influence on Electronic Transport Parameters

For the present example, we consider the following defect reactions: The thermal excitation of an electron-hole pair across a band-gap

$$0 \rightleftharpoons \mathrm{h}^{\bullet} + \mathrm{e}^{/} \tag{3.1}$$

[1]The Kröger-Vink-notation for point defects was introduced in 1956 [15]. In this notation, a point defect can generally be denoted as:

$$K_F^G$$

where F is the site of the defect, K the species on this site, and G the effective charge of species K on site F compared to a reference state. For example, $\mathrm{v}_{\mathrm{O}}^{\bullet\bullet}$ is a vacant ($K = \mathrm{v}$) oxygen site ($F = \mathrm{O}$), which has no absolute charge, so that it has a double positive *effective* charge as compared to a perfect reference state with O^{2-}. Another example is $\mathrm{Sr}_{\mathrm{La}}^{/}$, which is a strontium ion (formal charge Sr^{2+}) on a lanthanum site (formal reference charge La^{3+}), so that the strontium defect has a negative effective charge.

with the corresponding equilibrium constant

$$K_\mathrm{D} = p \cdot n = N_\mathrm{C} N_\mathrm{V} \cdot \exp -E_\mathrm{g}/\mathrm{k_B}T \tag{3.2}$$

and the formation of an oxygen vacancy, accompanied by the creation of two electrons to keep the charge balance:

$$\mathrm{O_O^X} \rightleftharpoons \mathrm{v_O^{\bullet\bullet}} + 2\mathrm{e}^{/} + \tfrac{1}{2}\,\mathrm{O_2}(g) \tag{3.3}$$

with the corresponding equilibrium constant:

$$K_\mathrm{R} = \frac{[\mathrm{v_O^{\bullet\bullet}}] \cdot n^2 \cdot \sqrt{p\mathrm{O_2}/p\mathrm{O_2^0}}}{\left[\mathrm{O_O^X}\right]} \tag{3.4}$$

with the standard pressure $p\mathrm{O_2^0} = 1\,\mathrm{atm}$. By expressing all concentrations in Eq. (3.4) as site fractions[2], we can relate K_R to the standard Gibbs energy ΔG^0 of the reaction.

$$K_\mathrm{R} = \exp\left(-\frac{\Delta G^0}{\mathrm{k_B}T}\right) = \exp\left(\frac{\Delta S^0}{\mathrm{k_B}}\right) \cdot \exp\left(-\frac{\Delta H^0}{\mathrm{k_B}T}\right) \tag{3.5}$$

where ΔH^0 and ΔS^0 are the standard enthalpy and entropy change. By further including the charge neutrality condition

$$2\,[\mathrm{v_O^{\bullet\bullet}}] + p = n + \left[\mathrm{C_B^{/}}\right] \tag{3.6}$$

and the site restriction

$$[\mathrm{v_O^{\bullet\bullet}}] + \left[\mathrm{O_O^X}\right] = [\mathrm{O}] \tag{3.7}$$

where [O] is the number of oxygen sites per formula unit (= 3 for the present example), we can, in principle, calculate the concentrations of all considered species, when K_D, K_R and the oxygen partial pressure $p\mathrm{O_2}$ are known. By simplifications of Eq. (3.6), known as the Brouwer approximations, simple functional dependencies of the different concentrations *vs.* $p\mathrm{O_2}$ can be obtained. This is sketched in Fig. 3.1. From the Brouwer diagram, we can see that, at high $p\mathrm{O_2}$, holes are the majority charge carrier, while at low $p\mathrm{O_2}$, electrons become dominating. In the following, we will focus on the implications of this p-n-transition on the electrical conductivity and the Seebeck coefficient. The total electronic conductivity

$$\sigma_\mathrm{Tot} = \sigma_\mathrm{p} + \sigma_\mathrm{n} = ne\mu_\mathrm{e} + pe\mu_\mathrm{p} \tag{3.8}$$

[2] For the electron concentration n, one often uses n/N_C as the site fraction, with N_C as the effective density of states in the conduction band.

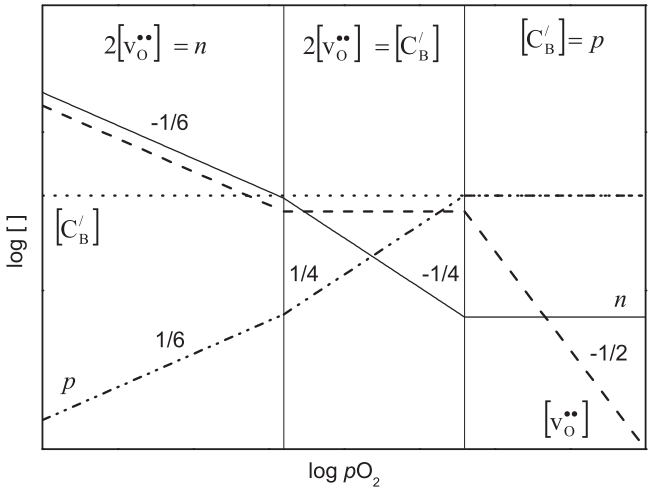

Figure 3.1: The defect concentrations against oxygen partial pressure in an oxide governed by the defect reactions (3.1) and (3.3). Three regions with different dominating majority defects are included.

generally undergoes a minimum when changing from an n- to a p-type region where the electronic and hole contribution to the total conductivity are equal:

$$\sigma_\mathrm{h} = \sigma_\mathrm{n} \tag{3.9}$$

For oxygen partial pressures well below and above the transition region, the conductivity follows the concentration of the majority carriers under the assumption that the carrier mobility does not depend on the concentration.

The Seebeck coefficient α of electrons or holes for a non-degenerate semiconductor can be written as (Eq. (2.39))

$$\alpha_n = -\frac{\mathrm{k_B}}{e} \cdot (\ln N_\mathrm{C}/n + A_\mathrm{n}) \tag{3.10}$$

$$\alpha_p = \frac{\mathrm{k_B}}{e} \cdot (\ln N_\mathrm{V}/p + A_\mathrm{h}) \tag{3.11}$$

where A_i are transport constants for electrons and holes. The total Seebeck coefficient is expressed by

$$\alpha_\mathrm{Tot} = \frac{\sigma_\mathrm{n}\alpha_\mathrm{n} + \sigma_\mathrm{p}\alpha_\mathrm{p}}{\sigma_\mathrm{n} + \sigma_\mathrm{p}} \tag{3.12}$$

The theoretical variation of σ_Tot and α_Tot as a function of $p\mathrm{O}_2$ for the present example is shown in Fig. 3.2. At high $p\mathrm{O}_2$, the charge carrier concentrations are independent of $p\mathrm{O}_2$ and α and σ are constant. When the hole concentration decreases, the absolute

value of α increases with a slope of $2.3 \cdot 86 \cdot \frac{1}{4}\,\mu\mathrm{VK}^{-1}$ per decade $p\mathrm{O}_2$, while $\log \sigma_{\mathrm{Tot}}$ decreases with a slope of $\frac{1}{4}$. By further reducing the hole concentration, the electron concentration becomes more and more dominant and α undergoes a sign change. In the low $p\mathrm{O}_2$ region, the Seebeck coefficient follows the concentration dependence via (3.10) and $\log \sigma_{\mathrm{Tot}}$ varies according to the concentration dependency of electrons as the majority carrier. These dependencies are indeed found in acceptor-doped $SrTiO_3$, when changing the oxygen partial pressure in a wide range [16, 17].

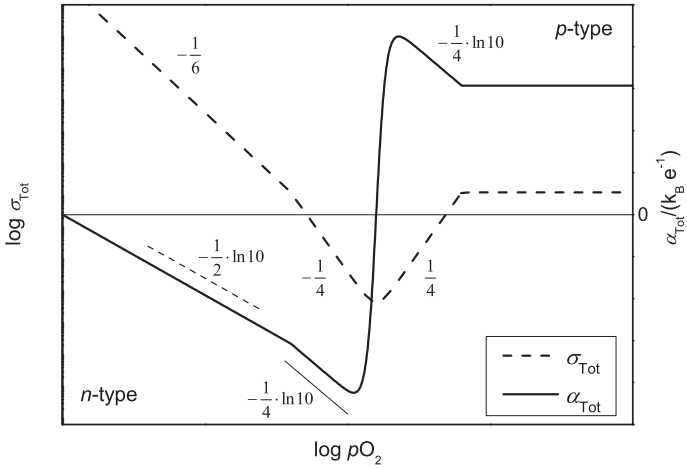

Figure 3.2: The total conductivity and the Seebeck coefficient of a non-degenerate semiconductor across the pn-transition. For reasons of simplicity, we choose $\mu_{\mathrm{n}} = \mu_{\mathrm{p}}$ and $A_{\mathrm{p}} = A_{\mathrm{n}} = 0$. The slope in the different regions reflects again the functional dependencies sketched in Fig. 3.1. When the electron concentration becomes too high, the non-degenerate approximation of the Fermi-Dirac-integrals is not valid anymore and the equations become inaccurate. For example, the calculated α_{Tot} turns positive again at the lowest $p\mathrm{O}_2$ (highest electron concentration), clearly showing the limitation of the employed formulae for high charge carrier concentrations.

Based on these equations, it is now in principle possible to extract relevant parameters from conductivity and Seebeck coefficient measurements, as for example the equilibrium constants of the defect reactions and the carrier mobilities.

3.2 Defect Chemistry of a Misfit Compound: Inherent Doping and Band-structure Representation

In this section, the analogy between the Kröger-Vink notation for defect species and the band-picture description will be shown. As an example, we choose the misfit-layered calcium cobaltite, which was studied in detail in Manuscripts 1 and 4. First, we want to give a short recapitulation of the developed defect chemical model using the Kröger-Vink notation. The structure is built up by two different subsystems stacked into each other: A layer of triangular, edge-sharing CoO_6-octahedra, referred to as the cobalt oxide layer (COL), and a layer of rock salt-type Ca_2CoO_3. The a and c lattice parameters of both subsystems are identical, but the b values differ ($b_{\mathrm{COL}}/b_{\mathrm{RSL}} = 0.62 = q$), leading to a structural modulation along that axis. As a pristine reference state, we choose $(Ca_2^{2+}Co^{3+}O_3)_q(Co_2^{x+}O_2)$, where $x = 4-q = 3.38$ to balance the overall charge. Both possible (or considered) states for a COL-cobalt site, an electron (represented by Co^{3+} when choosing a localised description) and a hole (corresponding to Co^{4+}) thus have an effective charge with respect to the reference state, which has a non-integer charge. Thereby, both species may be seen as defects and we denote them by

$$\mathrm{h}_{\mathrm{COL}}^{q\bullet} \text{ and } \mathrm{e}_{\mathrm{COL}}^{(1-q)/} \tag{3.13}$$

Two defect chemical reactions are considered: (a) the thermal excitation of hole carriers in the cobalt oxide layer, accompanied by a reduction of Co within the rock salt,

$$\mathrm{Co}_{\mathrm{RSL}}^{X} + \mathrm{e}_{\mathrm{COL}}^{(1-q)/} \rightleftharpoons \mathrm{Co}_{\mathrm{RSL}}^{/} + \mathrm{h}_{\mathrm{COL}}^{q\bullet} \tag{3.14}$$

and (b), the formation of oxygen vacancies within the rock salt layer, reducing the hole concentration within the cobalt oxide layer.

$$\mathrm{O}_{\mathrm{O,RSL}}^{X} + 2\mathrm{h}_{\mathrm{COL}}^{q\bullet} \rightleftharpoons \tfrac{1}{2}\mathrm{O}_2(g) + \mathrm{v}_{\mathrm{O,RSL}}^{\bullet\bullet} + 2\mathrm{e}_{\mathrm{COL}}^{(1-q)/} \tag{3.15}$$

To reproduce the experimental thermogravimetric data, we further restrict the formation of oxygen vacancies to sites next to Co^{2+}-sites.

How can this model be represented in a band structure description? Let us first review the tight-binding approach to understand the origin of the electronic bands. We consider N atoms far apart from each other, each with different atomic states ψ_i. The ψ_i are N-fold degenerate. When bringing the atoms closer together, the orbitals overlap and the degeneracy is lifted into a band of states. Still, the number of states within the band is N, i.e. depending on the number of considered atoms. We can now refer to the different bands according to their original state as 3s, 2p etc. Of

course, different bands can intersect in energy, so that a linear combination of orbitals has to be considered, leading to hybridization of the electronic states. However, it is still possible to project the state to its main constituent, so that we still keep the simple labeling of the different bands. By the same argument, it is justified that we can switch between the localised, ionic description and the delocalised band-picture, without changing the mathematical description[3]: The electronic wave function of a certain state can be projected onto a single atomic site when - as it is common in most transition metal oxides - it does not extend across large parts of the crystal.

The relevant states close to the Fermi level for oxygen are the 3 2p-orbitals, providing six electronic states per oxygen atom, where only four are occupied from "native" oxygen electrons. In metal oxides, the O:2p bands lie well below the Fermi-energy, so that the two empty states are filled by electrons from the metal species – making it to an O^{2-} site in an ionic description – while the metal becomes a positive ion.

The formation of an oxygen vacancy reduces the number of available states within the oxygen bands. There are many possible scenarios for the new, defective band structure, but in this simple model presented here we assume the bands to be rigid when oxygen vacancies are formed and that the only effect is a redistribution of electrons within the states. In all oxygen bands, the number of electronic states gets reduced when a vacancy is formed: In the 1s and 2s-band, the annihilated states can be thought of as being occupied by electrons native to the oxygen, which are also removed when forming the vacancy. In the case of the O:2p-bands, however, the two additional electrons stemming from the metal atoms have to be redistributed to empty states at the Fermi-level.

An effectively charged oxygen vacancy does not have a direct representation in a band picture description, because it simply does not contribute any electronic states. In fact, it can be thought of as annihilated states, which have been occupied by foreign electrons in the pristine state. The same is true for all defects with an effectively positive charge. In analogy, a metal vacancy (or a defect with an effectively negative charge) corresponds to annihilated states which have been empty under pristine conditions. Interstitials atoms increase the number of possible states within the relevant bands and can thus be treated in an analogue manner. Finally, thermal excitation of charge carriers (Eq. (3.1)) effectively empties states in a previously fully occupied band and partially fills a previously empty band. Since no atoms are removed, the total number of states does not change. In summary, the pristine state of "regular" materials is characterised by filled bands which all contain the same number of electronic states. Electronic defects for those materials correspond to partially filled bands. This can be either achieved by thermal excitation or by the

[3]However, the physical behaviour of both cases can be very different.

removal or insertion of atomic species, thereby varying the number of states within the respective bands.

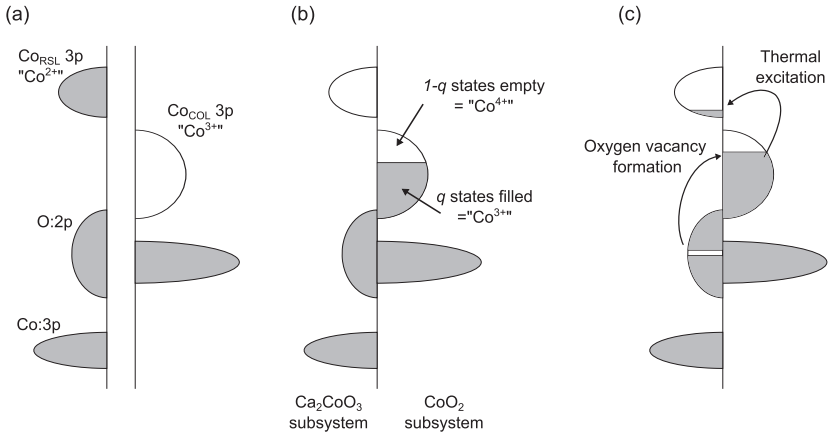

Figure 3.3: (a) A sketch of the band structure of CCO, where both subsystems are treated individually. In the Ca_2CoO_3 system (left), each band contains q states per formula unit, while bands in the CoO_2 layer (right) contain 1 state. (b) The same structure, but now electrons were allowed to redistribute across the two subsystems. The electrons from rock salt Co states now occupy states in the cobalt oxide layer of lower energy. Only a fraction q of the states in the band is occupied. (c) Band-diagram representation of the two processes considered in the defect chemical model for CCO: Thermal excitation moves electrons from a Co_{COL} state to a Co_{RSL} state. The creation of oxygen vacancies destroys states in an occupied oxygen band and the electrons are redistributed to states at the Fermi-level.

In CCO, it is now important to note that the number of each chemical species per formula unit $(Ca_2CoO_3)_q(CoO_2)$ is q for atoms from the rock salt subsystem, while for atoms in the cobalt oxide layer it is 1. Bands stemming from the rock salt layer thus contain less states than those associated with the cobalt oxide layer. If we assume that the highest occupied band stems from the cobalt oxide layer, this situation will always lead to partially filled bands, independent of the chosen reference state. This assumption is justified by both experimental [18, 19] and theoretical [20] findings. If on the other hand the highest occupied band would stem from the rock salt layer (which can be picturised by moving the empty COL-band in Fig. 3.3 (a) to very high energy), all Co ions within the rock salt layer would be in a 2+, Co ions in the cobalt oxide layer in a 4+ oxidation state and no partially filled bands were present.

But since charge transfer between the two subsystems occurs, the net charge of

the rock salt layer is positive, while the cobalt oxide layer carries a total negative charge. This results in a pristine state with a partially filled band, so that we can call the structure inherently defective. The band structure representation of the defect chemical model laid out by Eqs. (3.14) and (3.15) is sketched in Fig. 3.3.

In Na_xCoO_2 or other structures with an inherent deficiency on one sublattice, this dilemma of a defective reference state is solved by choosing a hypothetical, non-deficient state as pristine reference, e.g. $x = 1$ or $NaCoO_2$. The actual material with $x \neq 1$ is then treated as defective compared to the pristine state. Thus, the partially filled Co:3d band is explained by the formation of sodium vacancies, or in other words the annihilation of states within an empty band. The charge neutrality condition reads

$$\left[V'_{Na}\right] = [Co^{\bullet}_{Co}] \tag{3.16}$$

However, an analogue treatment of CCO would require the definition of a perfect reference state with $q = 1$, which – unlike the case $x = 1$ for sodium cobaltate – does not have a physical meaning. It is in this sense that misfit structures may be seen as the ideal example for the necessity of using a modified Kröger-Vink notation with fractional effective charges.

4 Review of Materials

In this chapter, the oxide materials most studied in a thermoelectric context are shortly reviewed, thereby motivating the choice of the particular materials investigated within this thesis. Special emphasis will therefore be given to the degree of oxygen nonstoichiometry in the different compounds. A more extensive review can be found in e.g. [21, 22].

4.1 Layered Cobaltites

In 1997, Terasaki *et al.* reported on the surprisingly high Seebeck coefficient of $Na_{0.5}CoO_2$, which was combined with a low, metallic resistivity [4]. The resulting power factor at room temperature was found to be even higher than that of the state-of-the-art thermoelectric material Bi_2Te_3. Na_xCoO_2 (NCO) exhibits a multitude of interesting properties, from charge ordering for $x = 0.5$ [23] to superconductivity in its hydrated form below 5 K [24], which have triggered intensive scientific activity on this material. It is fair to note, though, that water easily intercalates in between the layers, complicating the experimental handling of the samples and rendering the long time application in a non-encapsulated thermoelectric module difficult.

The origin of the high Seebeck coefficient found in NCO has been debated. Some authors claim that the Seebeck coefficient is dominated by the spin-orbital entropy, which can be described by a modified Heikes formula:

$$\alpha = -\frac{k_B}{e} \ln \beta \frac{x}{1-x} \tag{4.1}$$

where x is the concentration of Co^{4+}-holes moving on a background of $(1-x)$ Co^{3+} sites, and $\beta = g_3/g_4$ is the ratio of the local spin-orbital degeneracies of both ions [25, 26]. On the other hand, the high α was also explained by the classical Boltzmann transport theory, where a high effective mass was responsible for the coexistance of metallic conductivity and a high Seebeck coefficient [18, 27].

Contradicting results on the presence of a significant concentration of oxygen vacancies in Na_xCoO_2 can be found in the literature (e.g. [28–31]). Recently, it was proposed to explain the apparent oxygen loss of NCO at elevated temperature detected by thermogravimetry as the indication of a partial decomposition of the sample

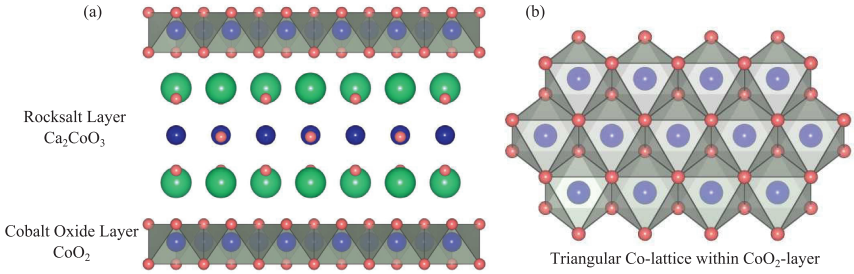

Figure 4.1: Crystal structure of $(Ca_2CoO_3)_q(CoO_2)$. (a) View along the a-axis. Layers of edge-sharing CoO_6-octahedra are separated by layers of Ca_2CoO_3 with a rock salt-type structure. (b) View along c. The triangular geometry of the Co-sites within the cobalt oxide layer is visible.

into CoO and Na_xCoO_2 with a higher sodium content x, rather than the formation of oxygen vacancies [32]. These results are in agreement with theoretical calculations [33].

A material which is closely related to NCO by sharing the same triangular CoO_2 layer, usually considered to be responsible for the metallic behaviour and the interesting electronic properties, is $(Ca_2CoO_3)_q(CoO_2)$ (CCO). Instead of a disordered Na-layer as for NCO, the CoO_2-layers in CCO are separated by a block of CaO-CoO-CaO with a rock salt-type structure. A sketch of the crystal structure of CCO is shown in Fig. 4.1. The ratio of the b-axes of both the cobalt oxide (COL) and the rock salt (RSL) subsystem gives an irrational number, leading to internal stress between the layers and to complicated misfit modulations of the sketched, "basic" crystal structure. The challenging structure of CCO is reflected in several detailed refinement studies (e.g. [34–36]).

In contrast to NCO, the capability of CCO to host a significant concentration of oxygen vacancies is generally accepted [37–39]. Shimoyama *et al.* report that the oxygen content in CCO - written as $Ca_3Co_4O_{9+\delta}$ - can be tuned in a range $0.15 < \delta < 0.36$ without decomposition of the structure [38]. Ling *et al.* refined the structures of oxygen-deficient and fully oxygenated samples and concluded that oxygen vacancies are exclusively formed within the central Co-O-layer of the rock salt subsystem, while the occupancies of other oxygen sites remain unchanged [40]. In Manuscript 1, we study the oxygen nonstoichiometry in CCO in a wide temperature and pO_2-range, propose a defect chemical model to describe our results, and discuss the charge transport properties of CCO as a function of the oxygen content. In Manuscript 4, we combine theoretical and experimental techniques to investigate the position of oxygen vacancies and the thermodynamics of the reduction in CCO.

Further, also misfit cobaltites with four rock salt-type layers separating the CoO_2-

layers have been found. In particular, one can find representatives without cobalt or another element with a variable valency within the rock salt layer (e.g. [41, 42]). The charge transfer between RSL and COL is thus only dependent on the misfit parameter and the oxygen content. Hébert *et al.* compared the properties of three structures $(Bi_{1.7}A_2O_4)_q(CoO_2)$ with $A = \mathrm{Ba},\ \mathrm{Sr},\ \mathrm{Ca}$ resulting in $0.5 \leq q \leq 0.61$ [43]. By preserving the electroneutrality, this will lead to a mixed-valent state within the COL, with a Co^{4+}- (or hole) concentration of

$$\left[\mathrm{Co}^{4+}\right] = 1 - \xi_{\mathrm{RSL}} \cdot q \tag{4.2}$$

where ξ_{RSL} is the charge of the rock salt layer per formula unit. For the given parameters, this corresponds to a Co^{4+}-concentration of 0.45 for $A = \mathrm{Ba}$ to 0.35 for $A = \mathrm{Ca}$. Indeed, a systematic variation of α and σ with q is observed. One should note, however, that small variations in the occupation of the Bi-sublattice will modify the charge balance between the two subsystems significantly, hindering a quantitative analysis. Still it is a good illustration of how the charge transfer between the electrostatically charged subsystems can be tuned by a variation of the misfit parameter q.

4.2 Delafossites

Delafossite compounds with a chemical formula AMO_2 show a layered structure, similar to the one of misfit cobaltites. A CdI_2-type layer of MO_6 octahedra is separated by a blocking layer of A atoms. Several compositions have been investigated, e.g. $M = \mathrm{Cr}, \mathrm{Fe}, \mathrm{Rh}$ and $A = \mathrm{Cu}$, showing power factors up to $6\,\mu\mathrm{WK}^{-2}\mathrm{cm}^{-1}$ at elevated temperatures [44, 45]. zT is however limited by a high thermal conductivity ($\kappa \approx 5 - 10\,\mathrm{Wm}^{-1}\mathrm{K}^{-1}$), which can be explained by the absence of a misfit relation between the two layers, effectively easing the phonon propagation. A possible approach to improve the thermoelectric performance is to induce disorder in one of the layers, thereby increasing the phonon scattering.

It is further known that - depending on the size of the M cation - oxygen can be intercalated into the A-layer, which will modify the electrical properties but might also be a way to decrease κ. Inconsistent reports on the possibility of intercalation in the delafossite compound with $M = \mathrm{Cr}$ and $A = \mathrm{Cu}$ can be found in the literature. While Maignan *et al.* claim the synthesis of $CuCrO_{2.5}$ in an ampoule under high oxygen pressure [46], Tate *et al.* report on decomposition of the sample when attempting to intercalate oxygen [47]. For clarification, we therefore decided to investigate possible oxygen nonstoichiometry in $CuCrO_2$. The undoped compound is insulating with a high resistivity at room temperature, but small amounts of Mg-doping ($x = 0.01$)

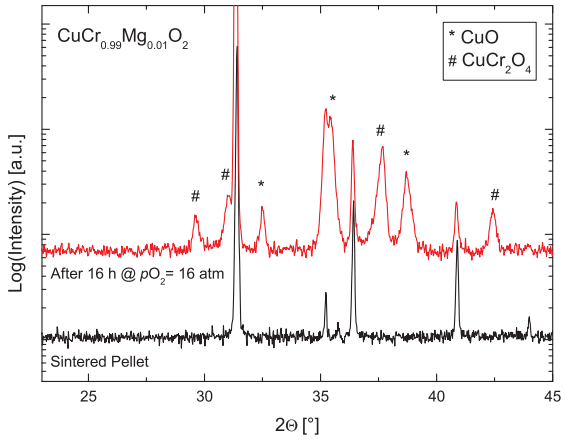

Figure 4.2: X-ray diffractogram of a sintered pellet before and after attempting oxygen intercalation. The weight increase is due to a decomposition into CuO and $CuCr_2O_4$ according Eq. (4.3).

lead to a significant improvement of the electrical properties. Thermogravimetry was used to check for possible under-stoichiometry, but no indication of a weight loss was found at 1000 °C and at oxygen partial pressures between 10^{-4} and 1 atm. The possibility of modifying the thermoelectric properties by intercalation of oxygen was investigated as well. We annealed the sample for 15 h at 550 °C, under an oxygen partial pressure of 16 atm. Indeed, a significant mass gain corresponding to an intercalated oxygen content of $CuCrO_{2.32}$ was observed. However, an X-ray diffractogram (Fig. 4.2) showed the partial decomposition into CuO and $CuCr_2O_4$ being responsible for the weight increase:

$$2CuCrO_2 + 2O_2 \rightarrow CuO + 2CuCr_2O_4 \tag{4.3}$$

4.3 Perovskites

Different perovskite materials ABO_3 have been investigated for thermoelectric purposes. The superior values of p-type cobaltites compared to their electron doped counterparts can be explained by the spin-orbital configuration of the considered Co-ions. Typically, at room temperature, Co^{2+} is in a high spin state ($t_{2g}^5e_g^2$), while Co^{3+} and Co^{4+} are found in a low spin state (($t_{2g}^6e_g^0$) and ($t_{2g}^5e_g^0$), respectively). In the electron doped case, a hopping of an electron from a Co^{2+}- to a Co^{3+}-site would result in an unfavourable intermediate spin configuration of Co^{2+} ($t_{2g}^6e_g^1$) and an intermediate spin state for Co^{3+} ($t_{2g}^5e_g^1$) [48]. In contrast, manganites exhibit a strong

Hunds-coupling, so that such spin-blockade effect are not expected to occur when Mn^{3+} electrons move on a background of Mn^{4+}-ions. In this context, several different manganites have been investigated as n-type thermoelectric material. Indeed, electron-doped $CaMnO_3$ is one of the most promising n-type thermoelectric oxides with a maximum zT-value of 0.3 at 750 °C [49].

The thermodynamics of the oxygen nonstoichiometry and its defect chemical description were studied previously [50, 51], but – even though oxygen vacancies were found to modify the thermoelectric properties of $CaMnO_3$ at high temperatures significantly [52, 53] – no systematic investigation of the influence of oxygen vacancies on the transport properties has been performed yet. In Manuscript 2 we showed that the charge carriers in $CaMnO_{3-\delta}$ move as strongly interacting small polarons and developed a model to understand charge transport in this and related materials at elevated temperatures.

Another well studied example with a perovskite structure is $SrTiO_3$, particularly interesting for the possibility to achieve p- and n-type doping. Finding the same host material for both n- and p-type leg is highly desirable when designing a thermoelectric module, due to a matching thermal expansion coefficient. However, the power factor in the p-type region is much lower than in the n-type – probably related to the sixfold degeneracy of the conduction band [54] – so that most investigations in a thermoelectric context focus on n-type materials. Okuda *et al.* reported a high powerfactor of $36\,\mu WK^{-2}cm^{-1}$ at room temperature, comparable to state-of-the-art material Bi_2Te_3 [55]. The figure of merit is however limited by a high thermal conductivity, which lead to intensive work on nanostructured STO ceramics, although no significant improvement of zT was achieved [56].

The influence of oxygen nonstoichiometry on the electronic transport properties of STO has already been studied during the 1980's and a classical, non-degenerate semiconducting behaviour was found, as described in section 3.1 (e.g. [16, 17, 57]).

Recently, a high thermoelectric performance of the related compound $EuTiO_3$ was reported by Sagarna *et al.*, reaching a zT of 0.4 at 775 °C [58]. In fact, the electrical properties are very sensitive to the oxygen content of this material. When the $EuTiO_3$ is annealed in highly reducing atmospheres, a small concentration of oxygen vacancies ($\delta \approx 0.015$) is formed, which are compensated by electronic charge carriers, leading to a change in conductivity by several orders of magnitude. These findings are published in Manuscript 2 within the list on page 37. The Eu^{2+} state is unfortunately highly unstable towards oxidation (Eq. (4.4)), making it difficult to prepare and control a sample with a well defined oxygen stoichiometry, as high temperatures and very reducing conditions are needed.

$$EuTiO_3 + \tfrac{1}{2}O_2 \rightarrow Eu_2Ti_2O_7 \tag{4.4}$$

4.4 Binary Oxides

Wide bandgap semiconductors like In_2O_3 and ZnO offer the possibility to tune the (n-type) charge carrier concentration in a wide range by doping with Sn and Al, respectively. The materials can thus be treated by the "classical" theory of degenerate semiconductors as reviewed in Chapter 2. In the case of ZnO, the best thermoelectric performance was reported to be $zT = 0.3$ at 1000 °C for $Zn_{0.98}Al_{0.02}O$ [59] and even 0.65 at 975 °C for $Zn_{0.96}Al_{0.02}Ga_{0.02}O$ [60]. However, the solubility of Al in ZnO is limited to small values of $x \approx 0.01$, while at higher doping, precipitates of $ZnAl_2O_4$ can be found, leading to an increase in the electrical resistivity.
The possible oxygen nonstoichiometry of $ZnO_{1-\delta}$ is assumed to be in the range of $\delta \approx 0.01 - 0.02$ [61,62] and it was shown that annealing in atmospheres with different pO_2 significantly modifies the electrical properties of the sample [63].

In_2O_3 is another well-studied oxide material for thermoelectric energy conversion similar to ZnO. The highest figure of merit is reported to be 0.46 at 1000 °C for $In_{1.8}Ge_{0.2}O_3$ [64]. Interestingly, the solubility of Ge in In_2O_3 is limited to $x \approx 0.01$, so that the reported composition is in fact a composite of doped In_2O_3 and precipitates of the pyrochlore $In_2Ge_2O_7$. Those precipitates are effectively lowering the thermal conductivity, leading to the observed, promising behaviour.

The defect chemistry of In_2O_3 is complex, including defect associates between indium- and oxygen interstitials acting as the electron donor. By reducing the sample, the concentration of these clusters is depleted and finally oxygen vacancies form up to a concentration of $\delta \approx 0.02$. Several studies report on the influence of the oxygen partial pressure on the conductivity (e.g. [65, 66]) and Seebeck coefficient [67] and their data are well described within a degenerate semiconductor model.

5 Experimental Methods

In Manuscript 3, we present and describe in detail the measurement apparatus used within this work for the electrical sample characterisation. In this chapter, some additional measurement techniques are presented and their use within this thesis is motivated. Where possible, this is done by including relevant results obtained during the work on this thesis, rather than by repeating the theory behind the respective techniques, which can be found in more appropriate depth in the relevant textbooks.

5.1 Sample Fabrication and Characterisation

All polycrystalline samples in this thesis were prepared by the standard solid state technique, in which powders of the precursor materials are thouroughly mixed in the desired ratio and subsequently calcined at high temperatures. The target compound forms via a surface reaction between the precursor materials and the reaction kinetics are thus usually limited by the solid-state diffusion of the different species to the grain surface. It is therefore advisable to use small-grained precursor powders and grind the powders in between the calcinations.

The fabrication of phase pure samples of $(Ca_2CoO_3)_q(CoO_2)$ was lengthy as discussed in Manuscript 1. Small deviations from the perfect Ca/Co ratio of 3/3.92, lead to the formation of a secondary phase, typically $Ca_3Co_2O_6$ or CoO. The latter is frequently overseen in standard XRD experiments as diffractograms are taken often using a copper X-ray source, leading to significant background enhancement due to both the fluorescence and the symmetrical crystal structure of CoO, resulting in few reflections in the investigated 2θ-range. These are further troubled by overlapping with reflections from $(Ca_2CoO_3)_q(CoO_2)$ and/or $Ca_3Co_2O_6$. In Fig. 5.1 we show the X-ray diffractogram of a powder sample of CCO with a Ca/Co-ratio of 3.95, which was calcined for 250 h at a maximum temperature of 850 °C with several intermediate grindings. The indexing is done via the notation ($\mathbf{h\ k_{RSL}\ k_{COL}\ l}$), reflecting the misfit nature of the structure and the requirement of a (at least) four dimensional space group to describe its symmetry. For comparison, a simulated diffraction pattern is shown for an approximated structure of CCO (Supercell (SC) of 13 units of the COL- and 8 units of the RSL subsystem; $q = 8/13 = 0.615$ and $b_{SC} = 8 \cdot b_{RSL}$). We used lattice parameters reported by Masset *et al.* [68], fractional coordinates

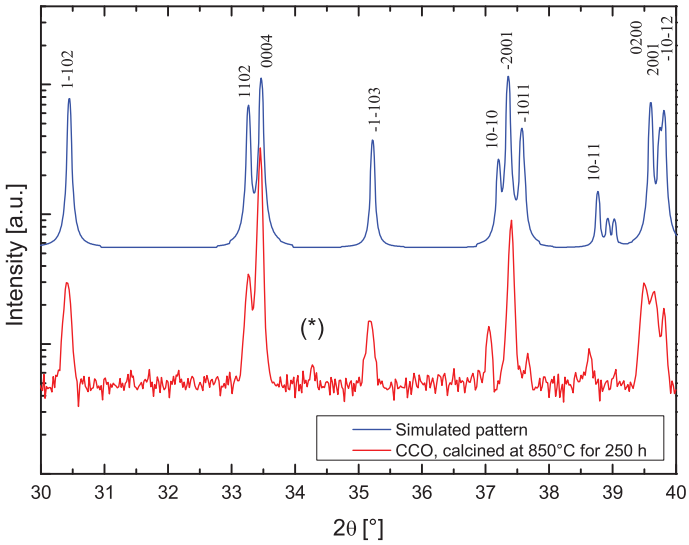

Figure 5.1: Detail from an X-ray diffractogram with long collection time (7 s per step) of CCO powder. (∗) corresponds to $Ca_3Co_2O_6$. For comparison, we have shown a simulated powder diffraction pattern for an approximated structural model of CCO.

from Miyazaki *et al.* [34], and pattern simulation was done using the PowderCell 2.4 software [69]. Due to the high resolution of the diffractometer (Bruker D8), the monochromaticity of the used wavelength (Cu K_{α_1}) and the long accquisition time (7 s per step), it is possible to resolve several reflections with very similar d-values. The observed and simulated intensity are not directly comparable as a preferential alignment of the platelike CCO-grains on the sample holder might be possible. This effect gets most pronounced in the pressed pellets. Despite the long calcination time, a small amount of an impurity phase ($Ca_3Co_2O_6$) could still be detected. As the weighed-in cation ratio predicts an excess of cobalt compared to the "perfect" CCO composition, this finding *per se* can be explained in two ways: (i) There is an additional small concentration of an (undetected) cobalt-rich phase (e.g. CoO) and the formation of CCO is not yet finished or (ii) cobalt gets evaporated during the calcination, leading to an excess of calcium in the remaining powder. However, as (XRD-)single-phase powders were obtained for similar calcination times and temperatures with a Ca/Co-ratio close to the nominal ratio of 3.92, we conclude that (a) is the more likely situation. A detailed study of the phase relations and solid solubility range in CCO can be found in [70].

To be able to perform electrical measurements on the material of choice, the syn-

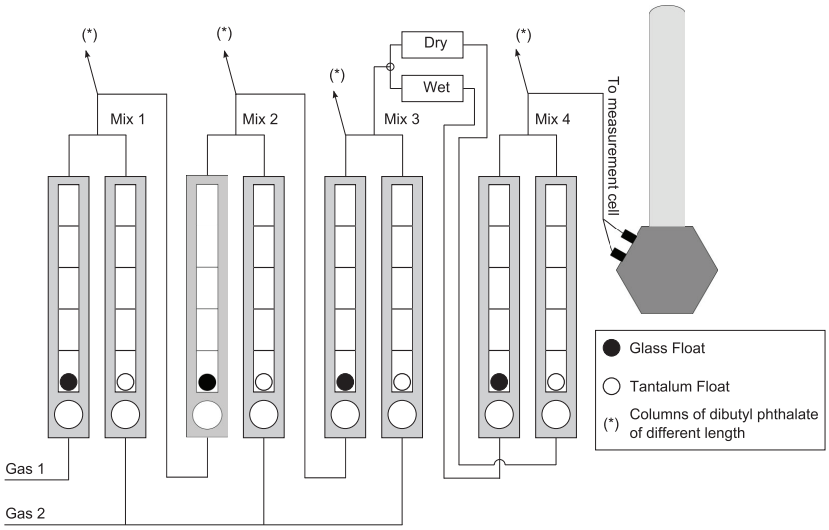

Figure 5.2: Schematic of the gas mixer used to control the atmosphere during electrical characterisation and thermogravimetric measurements.

thesised powder has to be compacted into a dense pellet. For a conventional sintering process, the calcined powder is isostatically pressed into a pellet at room temperature and sintered at high temperatures. For $CaMnO_3$ (Manuscript 2), this approach resulted in dense samples with a relative density (depending on the sintering temperature) between 80 and 95 %. Conventionally sintered pellets of CCO, however, reached a relative density of only 60-70 %, limiting the mechanical stability and reducing the electrical conducitivty of the sample.

The sample was therefore pressed isostatically at high temperatures to improve the densification process. The used hot-press allowed only a poor control of the sintering temperature and the oxygen partial pressure during sintering, which either resulted in a sample with a low relative density or led to the partial decomposition of the sample into CoO and $Ca_3Co_2O_6$. In the latter case, reoxidation of the sample by annealing at high temperatures in air resulted in a phase pure, dense pellet of relative densities beyond 90 %.

5.2 Gas Mixer and Measurement Cell

The electrical characterisation of the samples at high temperature was done in a commercial measurement cell (ProboStat, NorECs, Oslo, Norway), which was equipped with the setup described in detail in Manuscript 3. BNC-cables were used to monitor the signals of the electrodes used in electrical conductivity measurements. When

measuring the conductivity and the Seebeck coefficient in both sample orientations simultaneously, the internal heater to vary the in-plane temperature gradient was controlled by the shield of two of the BNC-cables. The cell was placed in a vertical tube furnace, which was controlled by a PID-regulator (Eurotherm 2216e or 3208) connected to one of the thermocouples within the cell. The atmosphere of the cell was controlled by an in-house built gas mixer as sketched in Fig. 5.2. Several rotameters (Sho-Rate 1355, Brooks Instruments) control the flow of the different gases. In most experiments presented within the thesis, gas 1 was oxygen, which was repeatedly diluted by gas 2, which was argon in the case of the electrical characterisation and helium for the thermogravimetric measurements. After each step, the excess gas not passed on to the next diluting step, is bubbled through columns of dibutyl phthalate, which also regulate the overpressure within the mixer.

After several diluting steps (three in the depicted gas mixer), the gas mixture can be dried or humidified. The experiments presented in this thesis were done under dry and oxidising conditions, where the obtainable range in the oxygen partial pressure pO_2 is limited by the O_2 residuals within the diluting gas 2 and the leakage of air into the mixer and cell, typically resulting in a minimal pO_2 of 10^{-5} atm. Wet gas is used to investigate the influence of water vapour on the electrical properties (e.g. in proton conductors) or to control the oxygen partial pressure precisely under reducing conditions, where the atmosphere contains H_2. In this case the pO_2 is determined by the equilibrium between oxygen, hydrogen, and water vapour

$$H_2 + \tfrac{1}{2}O_2 \rightleftharpoons H_2O \tag{5.1}$$

The partial pressure of water vapour is controlled by passing the gas through a saturated solution of KBr, resulting in a pH_2O of ≈ 0.025 atm at room temperature.

5.3 X-ray photoelectron spectroscopy

As discussed in Manuscript 1, the change in charge carrier concentration due to a variation of the oxygen content can be associated with a change in the average cobalt valency within the CoO_2-layer. A direct and preferably quantitative experimental assessment of this variation is therefore desired. X-ray photoelectron spectroscopy (XPS) is a powerful tool to determine the chemical state of the different species in a material, in particular the oxidation state. However, in the following, we will show that – under the temporal and instrumental limitations of this thesis – the XPS technique cannot be used to observe reliable changes in the cobalt oxidation states in CCO by a variation of the oxygen content.

The energetic shift for the different oxidations states of cobalt is unfortunately small

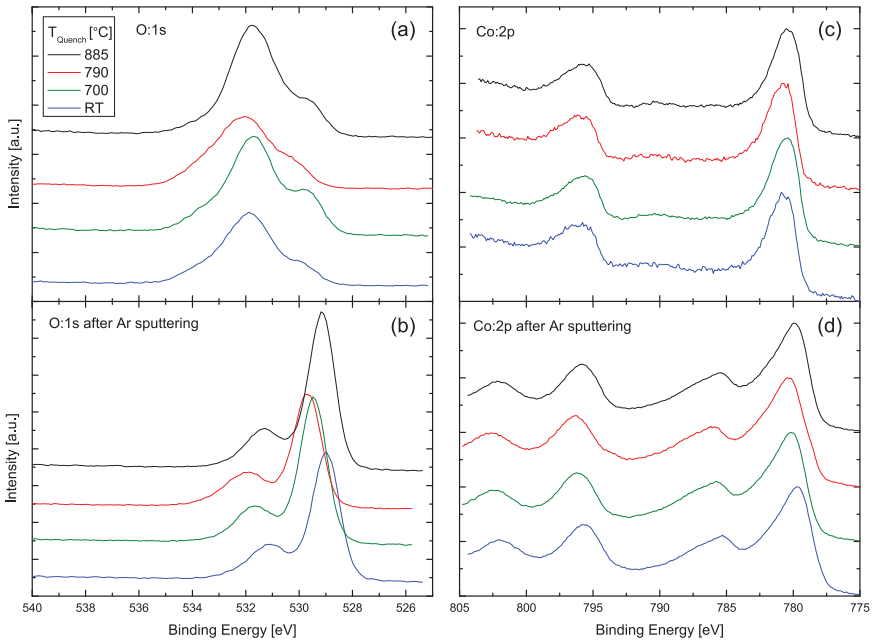

Figure 5.3: XPS spectra of polycrystalline CCO samples taken at room temperature. The spectra are vertically offset for clarity. (a)+(b) and (c)+(d) show the O:1s and Co:2p core level spectra before and after Ar sputtering, respectively. In both cases, no systematic variation of the spectra with δ could be observed. The different features of the spectra are significantly changed by sputtering, though.

and further complicated by several possible spin configurations. Still, some groups have investigated the variation of the XPS signal in CCO with doping or temperature (e.g. [71–73]). We have tried to observe a systematic variation of photoelectron spectra of CCO, when the concentration of oxygen vacancies is changed. We prepared a series of samples quenched after annealing at different temperatures in air. The XPS spectra of the O:1s and the Co:2p level are shown in Fig. 5.3. Wakisaka *et al.* assigned the two main components in the O:1s-spectra at 529 eV and 531.5 eV to contributions from the CoO_2- and the CaO-layer, respectively [71]. The high energy feature was further discussed as a sign of surface degradation due to oxygen loss. For our samples, the XPS O:1s intensity is dominated by the degradation component (Fig. 5.3 (a)), indicating that the as-quenched surface (despite careful polishing before annealing) is of too low quality to be used in an XPS experiment. Ion sputtering reduces the intensity of the degradation feature at 531.5 eV and restores the surface quality (Fig. 5.3 (b)). Still, in both cases, no systematic variation of

the spectra with δ could be observed. Analogously, non-systematic changes could be observed for the Co:2p core-level spectrum (Fig. 5.3(c)). Ion sputtering induces a reduction of the cobalt oxidation state, leading to a signifcant spectral contribution of Co^{2+}-species (compare to measurements of CoO-standards as reported in e.g. [74]).

5.4 Thermal Conductivity

The main focus within this thesis are the electrical transport properties – that is the electrical conductivity and the Seebeck coefficient – of oxides at high temperatures. The thermoelectric figure of merit further includes the thermal conductivity κ of the sample.

κ is typically measured by the laser flash technique [75]. Its measurement principle relies on the time it takes for a heat pulse, caused by a short laser pulse, to diffuse through a sample of thickness d. The temperature variation at the rear surface is measured as a function of time. The time $\tau_{1/2}$ it takes for this surface to reach half of its maximum amplitude is related to the thermal diffusivity by

$$D = 1.38\frac{d^2}{\pi^2 \tau_{1/2}} \tag{5.2}$$

The thermal diffusivity D is in turn related to the thermal conductivity κ by

$$\kappa = D\rho c_\mathrm{p} \tag{5.3}$$

where c_p is the heat capacity and ρ the density of the sample. Comparing the maximum amplitude ΔT_Max of a material with the one of a known reference material, further allows the calculation of the heat capacity c_p. We used a sample of Pyroceram 9606 as a reference. This material is a mixture of different oxides (mainly SiO_2 and Al_2O_3) [76] and was provided and characterised by Netzsch.

During the measurement, the sample chamber is flushed with nitrogen gas in the instrument. At high temperatures, we thus expect the uncontrolled formation of oxygen vacancies in our samples, modifying the experimental results. Alternatively, for a quenched sample, oxygen vacancies may be oxidised by residual oxygen within the atmosphere when the temperature is high enough. Still – as preliminary thermogravimetric results have given some understanding of the kinetics of reduction and oxidation – it is possible to measure the thermal conductivity of samples with different degrees of oxygen nonstoichiometry under effectively frozen conditions, given the experiment is done fast enough.

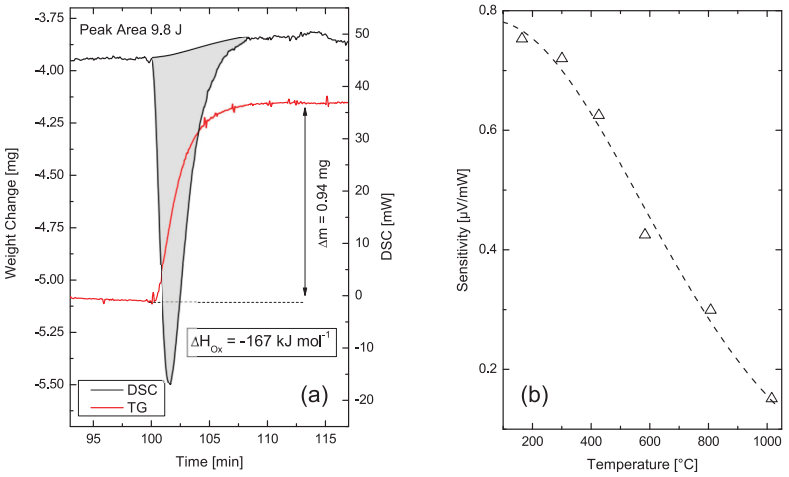

Figure 5.4: (a) TG and DSC signal when oxidising $CaMnO_{3-\delta}$ at 1000 °C. The oxidation enthalpy is determined to ΔH_{Ox} = -167 kJmol^{-1}. (b) The instrument calibration curve taken just before the measurement.

5.5 TG-DSC

In Manuscript 4, we use a method of combined calorimetry and thermogravimetry to determine the oxidation enthalpy of CCO directly, not relying on certain assumptions as when curve-fitting thermogravimetric data on the basis of a defect chemical model. The method is based on the simultaneous measurement of the heat and mass exchange during oxidation or reduction. The DSC signal reflects the heat flux from the sample to the instrument chamber as compared to a reference crucible. We have used a Netzsch STA 449 C Jupiter instrument. The gas atmosphere inside the measurement chamber was controlled by a gas mixer as described earlier. The TG-DSC technique has been established recently as a means to investigate the hydration thermodynamics of oxides [77], but so far it has not been used for oxidation experiments.

In order to assess the value of the TG-DSC technique as a quantitative tool for oxidation experiments, we started to investigate the oxidation of $CaMnO_{3-\delta}$, where the oxidation enthalpy within the cubic phase extracted from defect chemical modelling ($\Delta H_{\mathrm{Ox}} \approx -180\,\mathrm{kJmol^{-1}}$) [51] and coulometric titration ($\Delta H_{\mathrm{Ox}} \approx -165\,\mathrm{kJmol^{-1}}$) [50] was reported previously. In Fig. 5.4 (a), we show the TG-DSC signal of CMO at 1000 °C when the atmosphere was changed from a pO_2 of $\approx 5 \cdot 10^{-3}$ to 1 atm. The sample weight increases and an exothermic DSC signal is detected, both reflecting the filling of oxygen vacancies in the structure. It is interesting to note that the DSC-baseline shift is much smaller than the one observed when measuring at lower

temperatures (c.f. Manuscript 4), probably due to an increased influence of heat radiation. To convert the voltage signal of the DSC experiment into a meaningful heat flow, the sensitivity of the instrument has to be known. This is done by utilising the phase transition of several materials and comparing the DSC signal with the tabulated enthalpy. The sensitivity is then expressed as a polynomial fit:

$$s(T) = \left[P_2 + P_3 \cdot \frac{T - P_0}{P1} + P_4 \cdot \left(\frac{T - P_0}{P1} \right)^2 \right] \cdot \exp\left(- \frac{T - P_0}{P1} \right)^2 \tag{5.4}$$

The reference materials should be chosen to show a well characterised phase transition in the temperature range of interest. The most relevant reference materials and their corresponding transition temperature were ZrO_2 (1016 °C, [78]), $BaCO_3$ (808 °C, [79]), and K_2SO_4 (584 °C, [80]). For the oxidation enthalpy of cubic $CaMnO_{3-\delta}$, we obtain $167 \pm 15\,\mathrm{kJmol^{-1}}$, in excellent agreement with the reported values [50, 51]. The confidence interval given is the sum of the statistical error when averaging over different integration limits and different oxidation peaks, and the inaccuracy of the signal to heat flow conversion via the calibration curve.

6 List of Papers

The main findings during the work on this thesis are presented in four manuscripts:

Paper 1 – Electronic Transport Properties of $(Ca_2CoO_{3-\delta})_q(CoO_2)$
M. Schrade, H. Fjeld, T.G. Finstad, T. Norby
J. Phys. Chem. C, **118**, (2014), 2908-2918

Paper 2 – High Temperature Transport Properties of Thermoelectric $CaMnO_{3-\delta}$ – Indication of Strongly Interacting Small Polarons
M. Schrade, R. Kabir, S. Li, T.Norby, T.G. Finstad
J. Appl. Phys., **115**, (2014), 103705

Paper 3 – Versatile Apparatus for Thermoelectric Characterisation of Oxides at High Temperatures
M. Schrade, H. Fjeld, T. Norby, T.G. Finstad
submitted to Review of Scientific Instruments

Paper 4 – Oxygen Nonstoichiometry in $(Ca_2CoO_3)_{0.62}(CoO_2)$ - A Combined Experimental and Computational Study
M. Schrade, S. Casolo, P. Graham, C. Ulrich, S. Li, O.-M. Løvvik, T.G. Finstad, T. Norby
submitted to the Journal of Physical Chemistry C

In addition, I have contributed to the following manuscripts, which are not included in this thesis:

- **Signatures of electronic polarons in $La_{1-x}Sr_{1+x}MnO_4$ observed by electron energy-loss spectroscopy**, R. Kraus, M. Schrade, R. Schuster, M. Knupfer, A. Revcolevschi, B. Büchner, and J. Geck, *Phys. Rev. B*, **83**, (2011), 165130
- **Influence of the Oxygen Content on the Electronic Transport Properties of $Sr_xEu_{1-x}TiO_{3-\delta}$**, L. Sagarna, S. Populoh, A. Shkabko, J. Eilertsen, A. Maegli, R. Hauert. M. Schrade, L. Karvonen, A. Weidenkaff, *J. Phys. Chem. C*, **118**, (2014), 7821-7831
- **Studies of Optical, Electrical and Thermoelectric Properties of $BaPrO_3$**, A. Magrasó, A. Galeckas, M. Schrade, T.G. Finstad, T. Norby, *to be submitted*

6.1 Paper 1

Electronic Transport Properties of $(Ca_2CoO_{3-\delta})_q(CoO_2)$

M. Schrade, H. Fjeld, T.G. Finstad, T. Norby

J. Phys. Chem. C, **118**, (2014), 2908-2918

6.2 Paper 2

High Temperature Transport Properties of Thermoelectric $CaMnO_{3-\delta}$ – Indication of Strongly Interacting Small Polarons

M. Schrade, R. Kabir, S. Li, T.Norby, T.G. Finstad

J. Appl. Phys., **115**, (2014), 103705

High temperature transport properties of thermoelectric $CaMnO_{3-\delta}$ — Indication of strongly interacting small polarons

M. Schrade,[1,a)] R. Kabir,[2] S. Li,[2] T. Norby,[3] and T. G. Finstad[1]
[1]*Centre for Materials Science and Nanotechnology, Department of Physics, University of Oslo, Sem Sælandsvei 24, 0371 Oslo, Norway*
[2]*School of Materials Science and Engineering, University of New South Wales, Sydney, New South Wales 2052, Australia*
[3]*Centre for Materials Science and Nanotechnology, Department of Chemistry, University of Oslo, FERMiO, Gaustadalléen 21, 0349 Oslo, Norway*

(Received 31 January 2014; accepted 1 March 2014; published online 13 March 2014)

The conductivity and Seebeck coefficient of $CaMnO_{3-\delta}$ have been studied at temperatures up to 1000 °C and in atmospheres with controlled oxygen partial pressure. Both transport coefficients were varied *in situ* by the reversible formation of oxygen vacancies up to $\delta = 0.15$. The charge carrier concentration was calculated using a defect chemical model. The Seebeck coefficient could be approximated by Heikes' formula, while the conductivity shows a maximum at a molar charge carrier concentration of 0.25. These results were interpreted as a signature of strong electronic correlation effects, and it was concluded that charge transport in $CaMnO_{3-\delta}$ occurs via strongly interacting small polarons. General prospects for strongly correlated materials as potential candidates for high temperature thermoelectric power generation were discussed. © *2014 AIP Publishing LLC*.
[http://dx.doi.org/10.1063/1.4868321]

I. INTRODUCTION

Mixed-valent manganites with perovskite-related structures exhibit a rich variety of interesting electrical, structural, and magnetic properties and led to the development of new physical concepts like the superexchange mechanism and to new applications due to their pronounced magnetoresistive effect (see Ref. 1 for a review). Characteristic for these materials is a strong electron-phonon coupling, often leading to a self-localisation of charge carriers by lattice distortions. If the dimension of the carrier and its surrounding lattice distortion is in the range of the interatomic distance, it is named a small polaron and charge transport occurs via thermally activated hopping.[2]

Recently, manganites are also investigated as potential thermoelectric materials. Several classes of 3*d* transition-metal oxides such as layered cobaltites, titanates, or transparent conducting oxides are investigated as candidates for thermoelectric energy harvesting at high temperatures,[3–5] but despite considerable scientific activity within the field, the reported values for the thermoelectric figure of merit zT are still well below other state-of-the-art thermoelectric materials based on more scarce and/or environmentally harmful p-block elements. The highest zT-figures among oxides are reported for layered cobaltites as p-type conducting materials, while zT for n-type oxides is significantly lower (e.g., Ref. 6). Among these n-type thermoelectric oxides, electron doped $CaMnO_{3-\delta}$ is one of the most prominent n-type thermoelectric oxides with a reported maximum $zT = 0.3$ for $CaMn_{0.98}Nb_{0.02}O_3$,[7] making it a typical choice when designing an all-oxide thermoelectric generator.[8,9]

Although it is well established that the oxygen content in $CaMnO_{3-\delta}$ can be varied over a broad range making it an interesting material as a cathode in solid oxide fuel cells[10] or as an oxygen storage material in advanced combustion processes,[11] most of the published high temperature thermoelectric data are taken under atmospheric conditions with the oxygen content of the sample being poorly defined. Therefore, experimental data on nominally identical samples scatter significantly and show opposite temperature trends, and a profound assessment of these materials in thermoelectric applications is not yet possible (e.g., Refs. 12 and 13). Even when measuring in air, oxygen vacancies will form in $CaMnO_{3-\delta}$ and lead to a significant variation on thermoelectric properties at high temperatures.[14]

The defect chemistry of oxygen-deficient $CaMnO_{3-\delta}$ was recently studied by Goldyreva *et al.*[15] and will be summarized here. On the basis of thermogravimetric (TG) measurements, it was found that the defect properties of $CaMnO_{3-\delta}$ can be described by two chemical reactions: (a) The filling of oxygen vacancies accompanied by a oxidation of Mn-sites and (b) the thermal excitation of electronic charge carriers across the band-gap. In the Kröger-Vink-notation,[16] these reactions read

$$\frac{1}{2}O_2(g) + v_O^{\bullet\bullet} + 2Mn'_{Mn} = O_O^x + 2Mn_{Mn}^x, \quad (1)$$

$$2Mn_{Mn}^x = Mn'_{Mn} + Mn_{Mn}^{\bullet}. \quad (2)$$

Thermogravimetric data can be fitted with respect to the equilibrium coefficients for the reactions (1) and (2), K_{Ox} and K_D, respectively. Both reactions show an Arrhenius-type behaviour, where the oxidation reaction (Eq. (1)) is exothermic, while the charge disproportionation (Eq. (2)) is endothermic. The reaction enthalpies depend on the structural state of $CaMnO_{3-\delta}$.[15]

a)Electronic mail: matthias.schrade@smn.uio.no

 © 2014 AIP Publishing LLC

[This article is copyrighted as indicated in the article. Reuse of AIP content is subject to the terms at: http://scitation.aip.org/termsconditions. Downloaded to] IP: 129.240.152.45 On: Thu, 13 Mar 2014 16:04:41

In this paper, we report on our simultaneous measurements of Seebeck-coefficent and electrical conductivity of nominally undoped $CaMnO_{3-\delta}$ at high temperatures and in equilibrium with a well-defined atmosphere. Based on the previously published defect chemical model, we can calculate the concentration of all considered electronic species for the specific temperature and atmospheric composition, in particular the concentration of Mn^{3+}, which we identify with the molar charge carrier concentration x. We will further show that the strong correlation of small polaron charge carriers can lead to a simultaneous decrease in conductivity and Seebeck coefficient and discuss the general perspective for manganites with respect to thermoelectric application.

II. EXPERIMENTAL

Polycrystalline samples were synthesized via standard solid state reaction. Powders of $CaCO_3$ (≥99.0%, Sigma-Aldrich) and MnO_2 (≥99.0%, Sigma-Aldrich) were dried for 2 h at 150 °C and weighed in stoichiometric amounts. The mixed powders were ball milled and calcinated twice at 1000 °C for 24 h, with an intermediate grinding. The obtained powders were pressed into pellets at 100 MPa and sintered in air at 1300 °C for 24 h. Room-temperature X-ray diffraction data were collected using a Philips PANalytical X'pert MPD diffractometer using CuKα-radiation and a step-width of 0.02. All observed peaks could be indexed in agreement with literature[17] and no secondary phase could be detected (Fig. 1(a)). The lattice parameters were determined to $a = 5.30$ Å, $b = 7.47$ Å, and $c = 5.28$ Å (SG P*nma* (No. 62)). A bar-shaped sample of ca. $3 \times 3 \times 14$ mm^3 in dimension cut from the pellet was mounted into a commercially available measurement cell (ProboStat, NorECs, Norway), which was modified for our purposes (Fig. 1(b)): The sample was clamped into a spring-load system with an S-type thermocouple (PtRh10, Pt) attached on each side in good thermal and electrical contact with the sample. The Pt-leads of each thermocouple were used to measure the thermoelectric voltage across the sample. Two platinum electrodes were tightly wrapped around the sample serving as voltage probes during resistivity measurements. The cell was placed in a vertical tube furnace providing the base temperature of the measurement. The temperature difference across the two sample ends was stepwise varied using a resistive micro-heater placed underneath the sample. The measured thermoelectric voltage was corrected for Pt-lead contribution. The conductivity was measured in four point geometry, using the Pt-wires of the thermocouples as current leads and the two electrodes as voltage probes. The effects of Peltier heating and thermal offsets were taken care of by switching current direction. The oxygen partial pressure in the cell was controlled by diluting O_2 with Ar in a commercial gas mixer (ProGasMix, NorECs, Norway). The relaxation towards chemical equilibrium was monitored measuring the voltage across the two electrodes as a function of time when sending a constant current through the sample. All measurements presented here were taken at thermal and chemical equilibrium, unless otherwise noted.

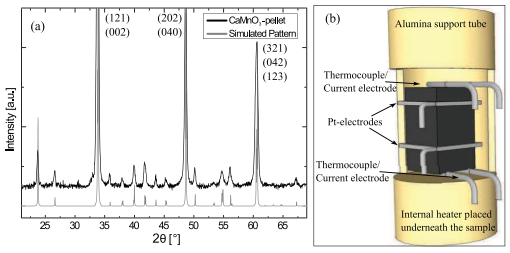

FIG. 1. (a) X-ray diffractogram of the as prepared sample. For comparison, we show a simulated pattern using the extracted lattice parameters and the structural model by Poeppelmeier *et al.*[17] All observed peaks could be indexed and no secondary phase could be detected. (b) The bar-shaped sample mounted into the measurement cell.

III. RESULTS AND DISCUSSION

Since the degree of oxygen non-stoichiometry is reported to vary only slightly over a large range of oxygen partial pressure at lower temperatures,[15] which agrees with our preliminary findings, we restrict our study to temperatures above 800 °C. The equilibrium oxygen nonstoichiometry, the electrical conductivity σ, and the Seebeck coefficient α as a function of temperature and oxygen partial pressure pO_2 are shown in Fig. 2. The negative sign of the thermopower indicates that electrons (here assumed to be localised as Mn^{3+}) are the dominating charge carrier in $CaMnO_{3-\delta}$. The values of σ and α at the highest oxygen partial pressure are in good agreement with literature data (e.g., Refs. 14, and 18–20). The influence of the extrinsic doping decreases when the concentration of oxygen vacancies increases. Therefore, the highest conductivity in Fig. 2(b) of 60 S cm^{-1} is almost identical with values found by Bocher *et al.* on a series of Nb-doped samples $CaMn_{1-x}Nb_xO_3$ with $0.02 < x < 0.08$.[14] The highest power factor $\alpha^2 \times \sigma$ was determined to 1.8 μW K^{-2} cm^{-1} at 900 °C and for an oxygen partial pressure of 1 atm. At higher temperatures and lower pO_2, the unusual doping dependence of the conductivity, discussed in this paper, leads to a significant reduction of the powerfactor (e.g., ≈1.0 μW K^{-2} cm^{-1} at 900 °C and pO_2 of 10^{-3} atm).

A. Influence of a structural phase transition on σ and α

Let us first consider the measurement taken at 800 °C. It is known, that $CaMnO_{3-\delta}$ undergoes a phase change from orthorhombic to tetragonal and finally to cubic when varying the oxygen partial pressure in the range used in the current experiment.[21] The region of existence of the tetragonal phase extends only over a narrow range in pO_2, so that no reliable defect chemical modelling is possible within this phase.

The conductivity and Seebeck coefficient vary linearly with $\log pO_2$ to an oxygen partial pressure of 0.01 atm, where the slope increases. To gain further insight on the influence of this sequence of phase transitions on the transport coefficients, we calculate the charge carrier concentration x as a function of the experimentally chosen pO_2 values via the defect chemical model presented in the introduction (Eqs. (1) and (2)) and by using the thermodynamic parameter K_D reported by Goldyreva *et al.*[15]

[This article is copyrighted as indicated in the article. Reuse of AIP content is subject to the terms at: http://scitation.aip.org/termsconditions. Downloaded to] IP: 129.240.152.45 On: Thu, 13 Mar 2014 16:04:41

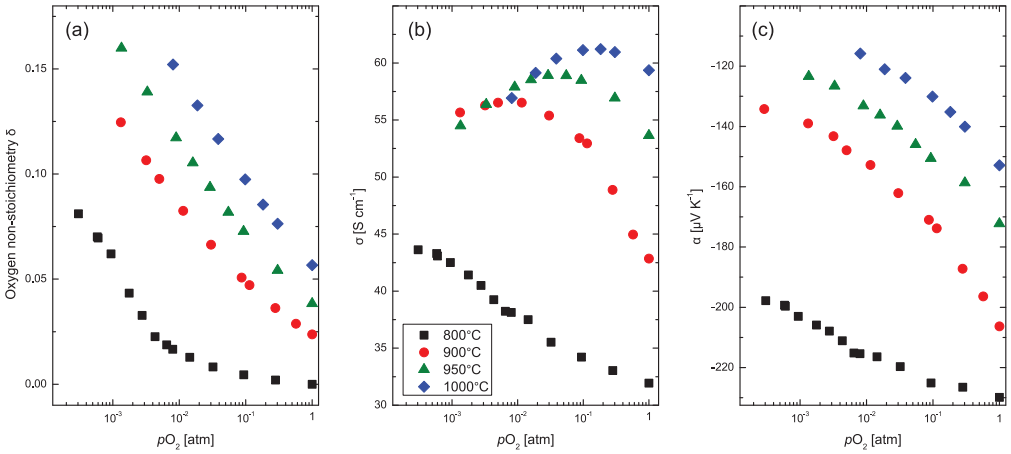

FIG. 2. (a) The oxygen nonstoichiometry δ, (b) the electrical conductivity σ, and (c) the Seebeck coefficient α of $CaMnO_{3-\delta}$ at different temperatures and oxygen partial pressures pO_2.

$$x = 2\delta + \frac{\delta + 2K_D - 4\delta K_D - \sqrt{K_D - 4\delta^2 K_D + \delta^2}}{4K_D - 1}, \quad (3)$$

where x is given as the site fraction of Mn^{3+} per formula unit of $CaMnO_{3-\delta}$. In Fig. 3, we plot the Seebeck coefficient α and the electron mobility μ, calculated by the standard expression

$$\sigma = x\mu Ze, \quad (4)$$

with $Z \times e$ being the charge of each carrier. The Seebeck coefficient α changes steeply with charge carrier concentration in the orthorhombic phase and flattens out in the cubic phase. A widely used high temperature limit for the Seebeck coefficient in localized hopping conductors is the Heikes formula[22,23]

$$\alpha = -\frac{k_B}{e} \times \ln\left[\frac{g_3}{g_4} \times \frac{1-x}{x}\right]. \quad (5)$$

The $g_i = g_{Spin} \times g_{Orbital}$ are the spin and orbital degeneracies of a Mn^{i+}-site. In the cubic phase, the two e_g- and the three t_{2g}-orbitals are degenerate, while in the orthorhombic phase, this degeneracy is lifted. Due to the strong Hund's coupling of Mn-d-electrons, we only consider high-spin configurations here. In the orthorhombic crystal field, the respective factors in Eq. (5) are $g_3 = g_{Sp} \times g_{Or} = 5 \times 1 = 5$ and $g_4 = g_{Sp} \times g_{Or} = 4 \times 1 = 4$, while in the cubic phase, both e_g-orbitals can be occupied and $g_3 = g_{Sp} \times g_{Or} = 5 \times 2 = 10$, while $g_4 = 4$ remains unchanged. This analysis predicts an increase of $|\alpha|$ by $60\,\mu$V/K when going from the orthorhombic to the cubic phase, independent of the charge carrier concentration x. However, the discrepancy with our observation of a rather continuous change in α can be explained by an energetic splitting of the e_g-orbitals in the orthorhombic phase in the order of k_BT, making both e_g-orbitals thermally accessible, so that the number of available states and thus g_3 do not change when entering the cubic phase.

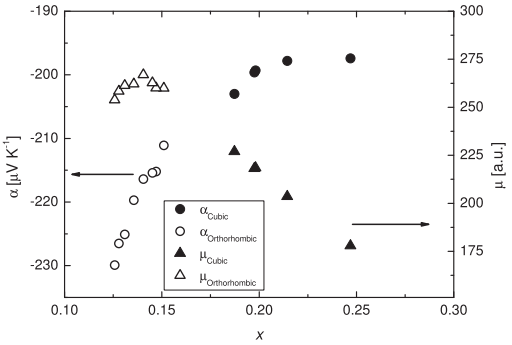

FIG. 3. Mobility μ and Seebeck coefficient α as a function of calculated charge carrier concentration x at 800 °C. No stepwise behaviour can be observed across the phase transition in any of the plots.

In addition, also the carrier mobility calculated from the conductivity via Eq. (4), does not show a discontinuous change across the phase transition (Fig. 3). The mobility of (localised) charge carriers is—in general—a sensitive function of the orbital overlap and thus of the bond-angle of neighbouring species. In the cubic phase of $CaMnO_{3-\delta}$, the angle of a Mn-O-Mn-bond is 180°, while it deviates from that in the tetragonal and orthorhombic phase. Our observation of a continuous change can be explained by a gradual relaxation of this angle to 180° when oxygen vacancies are formed, in agreement with a structural study.[14] However, a clear difference is seen in the variation of μ with carrier concentration x: While $\mu(x)$ appears to be almost constant in the orthorhombic phase and the corresponding low carrier concentrations, it shows a linear decrease in the cubic phase and higher x. This strong decrease cannot be explained by changes in the structure of $CaMnO_{3-\delta}$, which should lead to an increased mobility in the cubic phase, but another mechanism has to be considered.

B. Transport properties in the cubic phase

At higher temperatures, $CaMnO_{3-\delta}$ is in the cubic phase for most of the pO_2-range studied and no discontinuous

[This article is copyrighted as indicated in the article. Reuse of AIP content is subject to the terms at: http://scitation.aip.org/termsconditions. Downloaded to] IP: 129.240.152.45 On: Thu, 13 Mar 2014 16:04:41

behaviour of δ is reported in the literature. The absolute value Seebeck coefficient decreases continuously with increasing δ as it is expected for an increasing charge carrier concentration while the conductivity goes through a broad maximum. This is an unusual result as α and σ generally vary diametrally as a function of charge carrier concentration. To investigate this behaviour in more detail, we again plot α, σ, and μ against the carrier concentration calculated from the defect chemical model (Fig. 4). At the highest measured temperatures, the Seebeck coefficient shows only a weak dependency on temperature and Heikes formula should thus be an appropriate model. Indeed, the calculated curve by Eq. (5) reproduces the magnitude and change of the experimental data to a certain degree, as seen in Fig. 4(c).

If one includes the hitherto neglected population of Mn^{5+} as a possible site for an electron to hop to with a degeneracy $g_5 = g_{\mathrm{Orbital}} \times g_{\mathrm{Spin}} = 3 \times 3 = 9$, one can calculate the Seebeck coefficient by the weighted average of the two contributions[24]

$$\alpha = -\frac{k_B}{e}\left[\frac{[Mn^{5+}]}{[Mn^{5+}]+[Mn^{4+}]} \times \ln\left(\frac{10}{9}\times\frac{1-x}{x}\right) + \frac{[Mn^{4+}]}{[Mn^{5+}]+[Mn^{4+}]} \times \ln\left(\frac{10}{4}\times\frac{1-x}{x}\right)\right]. \quad (6)$$

The result slightly improves the agreement between calculation and experiment as indicated by the dashed line (calculated for 1000 °C in Fig. 4(c)).

The occurrence of a maximum in conductivity at around $x = 0.24$, which is via Eq. (4) equivalent to a strong decrease of the mobility μ with x (Fig. 4(b)) is more puzzling. It has been observed previously that the conductivity of $CaMnO_{3-\delta}$ at room temperature varies nonmonotoneously with increasing δ.[25] Those authors attribute this behaviour to an ordering of oxygen vacancies accompanied by an ordering of Mn^{3+} and Mn^{4+} species. In this model, electron transport occurs along these charge-ordered stripes, whose density reaches a maximum at $\delta = 0.16$. However, charge ordering is an unlikely scenario at the high temperatures studied within the present work and the maximum conductivity is observed for a δ-value around 0.08, for which no vacancy ordering has been reported (cf., e.g., Ref. 26). As the employed Heikes formula is derived for the case $U \gg k_B T$, where the high on-site repulsion prevents the double occupancy of one Mn-site by two electrons, we suggest the following qualitative model: With increasing oxygen vacancy concentration δ, the number of charge carriers increases to maintain charge neutrality, but at the same time, the number of available sites get reduced

$$\sigma \propto (1-x) \times x. \quad (7)$$

This model has been employed by several authors previously to describe the doping dependency of small polaron hopping conductors (e.g., Refs. 27 and 28). However, it predicts a maximum in conductivity at $x = 0.5$, while the experimental observations for electrons in $CaMnO_{3-\delta}$ (this study) and holes in $La_{1-x}Ca_xMnO_3$[28] find a maximum around $x = 0.25$. Apparently, the simple model in Eq. (7) provides an intuitive tool to reproduce the unusual doping dependency of transport coefficients in $CaMnO_{3-\delta}$, but a more sophisticated model, including more interaction terms than nearest-neighbour Coulomb repulsion, is needed to fully understand the present observation. Assuming that one electron spreads over two lattice sites may well describe the observed conductivity maximum around $x = 0.25$ within Eq. (7) but fails to reproduce the $\alpha(x)$-curve as calculated by Heikes' formula.

Ciuchi and Fratini have recently derived a cluster model to describe the mobility of small polarons interacting via long-range Coulomb forces.[29] In their theory, the mobility of interacting small polarons can be written as

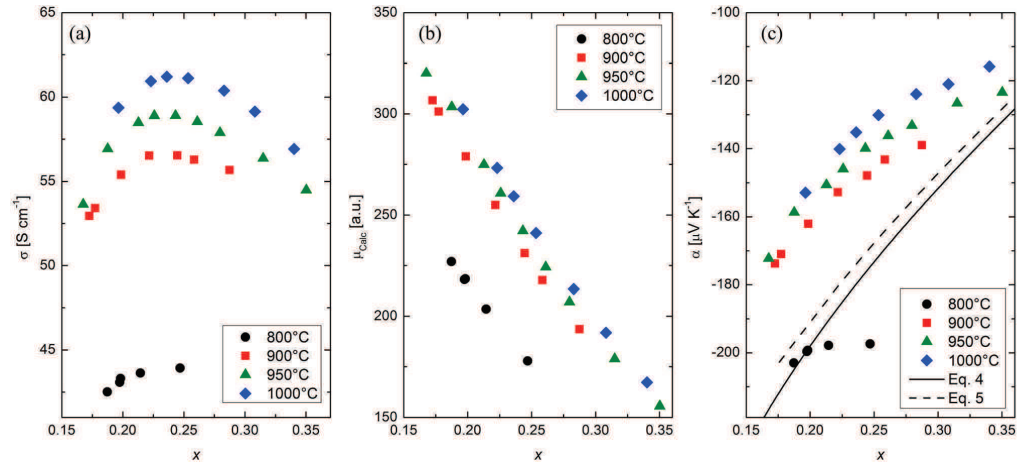

FIG. 4. The electrical conductivity σ (a), the calculated carrier mobility μ (b), and the Seebeck coefficient α (c), in the cubic phase of $CaMnO_{3-\delta}$ as a function of carrier concentration x. σ shows a maximum for $x \approx 0.25$ (a), implying a strong decrease of μ with increasing x via Eq. (4) (b). α can be roughly described by Heikes' formula (c).

[This article is copyrighted as indicated in the article. Reuse of AIP content is subject to the terms at: http://scitation.aip.org/termsconditions. Downloaded to] IP: 129.240.152.45 On: Thu, 13 Mar 2014 16:04:41

$$\mu = \frac{A}{T} \times \exp\left(-\frac{E_a}{k_B T}\right) \times \exp\left(-\frac{E_\xi \times x}{k_B T}\right). \quad (8)$$

If charge transport takes place in three dimensions, E_ξ is given as

$$E_\xi = \frac{\pi e^2}{3\epsilon_0 \times \epsilon_r} \times a^2. \quad (9)$$

A in Eq. (8) comprises parameters like the number of neighbours, the hopping distance, and the hopping attempt frequency and E_a is the activation energy for an electron to hop. In Eq. (9), a is the distance between two polaron sites and ϵ_r is the dielectric permittivity. The introduction of oxygen vacancies not only changes the concentration of electrons in the system but also decreases the effective number of nearest neighbours (both occupied and unoccupied ones), as hopping is only possible if the orbital overlap within the Mn-O-Mn-bridge is finite. It is therefore reasonable to assume $A = (3-\delta) \times A^*$. An additional factor $(1-x)$ compared to Eq. (8) ensures that the mobility is 0 when all manganese sites are filled ($x = 1$). We rewrite the expression for the mobility

$$\mu^*(x) = \frac{\mu_{Calc}}{3-\delta} = B \times (1-x) \times \exp\left(-\frac{E_\xi \times x}{k_B T}\right), \quad (10)$$

with $B = \frac{A^*}{T} \times \exp(-\frac{E_a}{k_B T})$. One can see that the mutual repulsion of the polarons ($E_\xi \neq 0$) leads to an effective gradual increase of the apparent activation energy with increasing carrier concentration x. Eq. (10) describes our data to a high degree (Fig. 5), and the corresponding fitting parameters are given in Table I. Both parameters B and E_ξ increase with temperature.

The increase of E_ξ (Eq. (9)) is likely to be due to a decrease of the relative permittivity ϵ_r, rather than a significant increase in hopping distance a. ϵ_r (or the electric polarizability) generally decrease at higher temperatures due to an increased thermal motion of the charged species. From the temperature dependence of the parameter B, it is possible to calculate an estimate of the polaron activation energy

TABLE I. Fitting parameters according to Eq. (10).

Temperature (°C)	B (a.u.)	E_ξ (meV)
800	156	241
900	193	249
950	198	257
1000	210	276

without any correlations present (for example, realised in a sample with very low charge carrier concentration). We obtain 0.28 ± 0.02 eV (Fig. 6). The increase of the apparent activation energy for the present carrier concentrations due to the correlation effect is in the range of $E_\xi \times x \approx 60$ meV.

To conclude the preceding paragraph, we state that the conductivity in $CaMnO_{3-\delta}$ within the cubic phase can be described by small polarons with strong mutual Coulomb repulsion. This behaviour is likely to occur similarly in other related calcium manganite samples with donor dopants as the source for electronic charge carriers instead of oxygen vacancies as in this work. The total apparent activation energy agrees well with the value recently reported in a similar study.[30]

Fast cooling or quenching a sample from a high temperature state with well defined oxygen partial pressure provides a means to obtain samples with a constant δ at lower temperatures. A sample which has been repeatedly prepared in such way is expected to vary only in δ and thus in charge carrier concentration, while other parameters like the unintended doping level, the electronic band gap, the hopping activation energy, or the interatomic distance remain approximately the same. A variation in the apparent hopping activation energy for one sample with different δ can thus be attributed to the mutual repulsive interaction of small polarons as discussed above. Therefore, we annealed one sample at high temperature and in atmospheres with different pO_2, quenched it, and measured the transport properties up to 450 °C. Preliminary thermogravimetric experiments have shown that $CaMnO_{3-\delta}$ is kinetically stable towards reoxidation below ≈ 500 °C. All

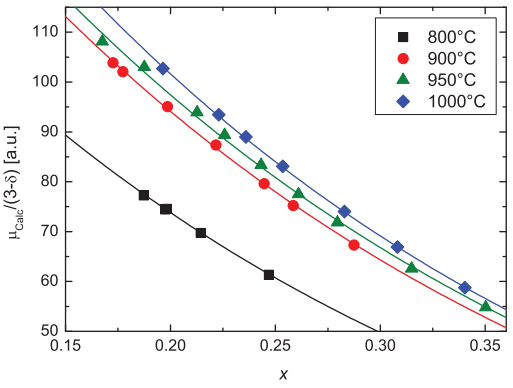

FIG. 5. The normalised mobility in the cubic phase of $CaMnO_{3-\delta}$ vs. calculated carrier concentration. Lines represent the numerical fit via Eq. (10).

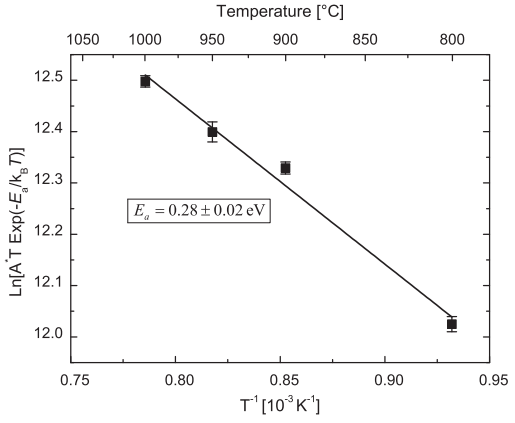

FIG. 6. Arrhenius-type plot of the prefactor B to extract the hopping energy in the absence of electronic correlation.

[This article is copyrighted as indicated in the article. Reuse of AIP content is subject to the terms at: http://scitation.aip.org/termsconditions. Downloaded to] IP: 129.240.152.45 On: Thu, 13 Mar 2014 16:04:41

measurements have been performed on the same sample, quenched from thermodynamic conditions where $CaMnO_{3-\delta}$ is within the cubic phase. As the dense ceramics obtained as described in the Experimental section are prone to develop small cracks due to the thermal stress under quenching, we used a sample sintered at 1100 °C and with a relative density of 75% for this experiment. Reproducibility and internal consistency were confirmed by several repeated heating-quenching cycles. The conductivity decreases with increasing δ and can be described by an activated hopping process for all studied values of δ (Fig. 7). The activation energy increases with increasing δ or charge carrier concentration. In this temperature regime, the carrier concentration is dominated by carriers induced due to oxygen vacancies, and contributions from thermal excitation via Eq. (2) can be neglected. The absolute value of the activation energy around 0.2 eV is less than expected from our high temperature results, where the correlation-free activation energy was determined to be 0.28 eV. On the other hand, the variation in activation energy of 100 meV due to the mutual repulsion of charge carriers is higher than estimated from the high temperature results (via Eq. (10) with $E_\xi \approx 250$ meV and $x = 2 \times \delta$). However, the obtained values agree well with a study of the hole-conductor $La_{1-x}Ca_xMnO_{3-\delta}$.[31] The discrepancy could, for example, be related to an anomaly in resistivity of $CaMnO_{3-\delta}$ around 700 K,[19,32] possibly indicating a different transport mechanism, for example, large polarons, at lower temperatures. In any case, despite an increase in charge carrier concentration by the introduction of oxygen vacancies, the conductivity decreases with δ, indicating a strong interaction of charge carriers.

Finally, we want to discuss shortly the implications of the presented model in the search for new thermoelectric materials. It is instructive to investigate the numerator in zT, the power factor $\alpha^2 \times \sigma$, rather than treating α and σ individually. For the simple model proposed, the power factor can be calculated by combining Eqs. (4), (5), and (10)

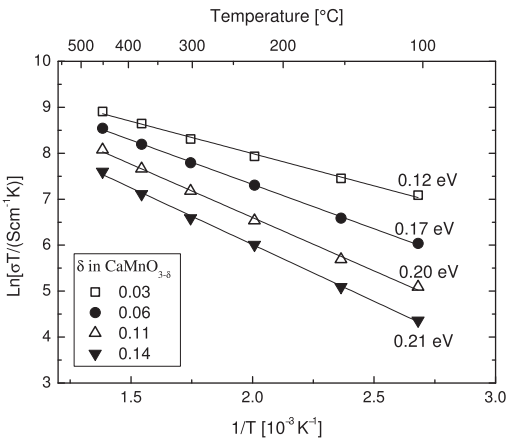

FIG. 7. $\ln \sigma T$ vs. $1/T$ for a sample with different oxygen vacancy concentration. The activation energy increases with increasing δ (or charge carrier concentration).

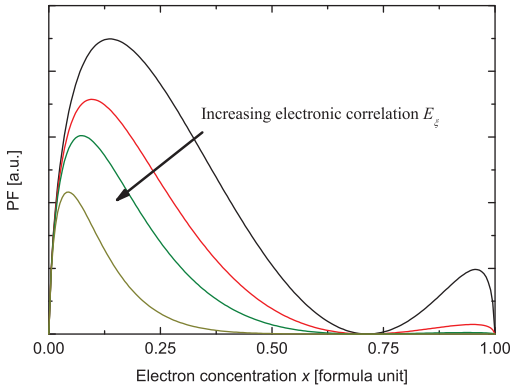

FIG. 8. The power factor $\alpha^2 \times \sigma$ as a function of carrier concentration and for different correlation strengths E_ξ.

$$\alpha(x)^2 \times \sigma(x) \propto \ln\left(\beta \times \frac{1-x}{x}\right)^2 \times \exp(-E_\xi \times x) \times (1-x) \times x, \tag{11}$$

and is schematically shown in Fig. 8. Increasing the strength of mutual Coulomb repulsion via an increase in the parameter E_ξ shifts the maximum of the power factor to lower carrier concentrations or doping levels. Further, does the maximum of the power factor get reduced when other parameters like the bandwidth are kept constant. But the most severe implication of the increased electronic correlation is that the concentration range with $PF(x) \geq PF_{\mathrm{Max}}/2$ gets narrower with increasing E_ξ. In materials with a non-constant carrier concentration, e.g., by intrinsic, thermal excitation like in $CaMnO_{3-\delta}$ and its doped compounds, this will lead to a rather sharp peak in zT vs. temperature, thus narrowing the temperature range of optimal performance and finally limit the potential applicability of materials with strong Coulomb repulsion in thermoelectric generators. However, there is experimental evidence for a variable optimal doping concentration (ranging from 0.02 to ≈0.10) for different dopants in $CaMnO_{3-\delta}$, possibly indicating that the strength of correlations depends on the doped species.[7,33]

IV. SUMMARY

In conclusion, we have studied the influence of oxygen non-stoichiometry on the high temperature transport properties of $CaMnO_{3-\delta}$. It is shown that the oxygen stoichiometry in $CaMnO_{3-\delta}$ can be reversibly varied within a broad range up to $\delta = 0.15$ at high temperatures and in different atmospheres allowing significant *in situ* doping of the material. The thermoelectric properties change significantly with varying δ. With increasing δ, an unusual simultaneous decrease of both conductivity and absolute magnitude of Seebeck coefficient is observed. This behaviour can be explained by a conduction process in $CaMnO_{3-\delta}$ at high temperatures via strongly interacting small polarons. The mutual Coulomb repulsion of these polarons quickly reduces the mobility once charge carriers are introduced into the system. The total

[This article is copyrighted as indicated in the article. Reuse of AIP content is subject to the terms at: http://scitation.aip.org/termsconditions. Downloaded to] IP: 129.240.152.45 On: Thu, 13 Mar 2014 16:04:41

activation energy of transport at high temperatures of 0.34 eV was disentangled to consist of two parts: One to be 0.28 eV for $CaMnO_{3-\delta}$ with a negligible carrier concentration and an additional energy $E_{Corr} = E_{\xi} \times x$ due to electronic correlations with E_{ξ} around 0.25 eV and x being the molar charge carrier concentration. The Seebeck coefficient in the studied temperature and carrier concentration range can be described by Heikes' formula to a satisfactorial degree. The present study shows that both thermoelectrical characterisation as well as fundamental analysis of the transport processes in oxides benefit from the careful control of oxygen content.

ACKNOWLEDGMENTS

The authors gratefully acknowledge funding by the Research Council of Norway within the THERMEL Project (143386).

[1]J. M. D. Coey, M. Viret, and S. von Molnár, Adv. Phys. **48**, 167 (1999).
[2]N. Mott and E. Davis, *Electronic Processes in Non-crystalline Materials*, edited by W. Marshall and D. Wilkinson (Clarendon Press, Oxford, 1979).
[3]I. Terasaki, Y. Sasago, and K. Uchinokura, Phys. Rev. B **56**, R12685 (1997).
[4]K. Koumoto, R. Funahashi, E. Guilmeau, Y. Miyazaki, A. Weidenkaff, Y. Wang, and C. Wan, J. Am. Ceram. Soc. **96**, 1 (2013).
[5]S. Hébert and A. Maignan, "Thermoelectric oxides," in *Functional Oxides* (John Wiley & Sons, Ltd, 2010), pp. 203–255.
[6]J. W. Fergus, J. Eur. Ceram. Soc. **32**, 525 (2012).
[7]L. Bocher, M. H. Aguirre, D. Logvinovich, A. Shkabko, R. Robert, M. Trottmann, and A. Weidenkaff, Inorg. Chem. **47**, 8077 (2008).
[8]I. Matsubara, R. Funahashi, T. Takeuchi, S. Sodeoka, T. Shimizu, and K. Ueno, Appl. Phys. Lett. **78**, 3627 (2001).
[9]P. Tomeeš, C. Suter, M. Trottmann, A. Steinfeld, and A. Weidenkaff, J. Mater. Res. **26**, 1975 (2011).
[10]E. Tsipis and V. Kharton, J. Solid State Electrochem. **12**, 1367 (2008).
[11]H. Leion, Y. Larring, E. Bakken, R. Bredesen, T. Mattisson, and A. Lyngfelt, Energy Fuels **23**, 5276 (2009).
[12]J. Park, D. Kwak, S. Yoon, and S. Choi, J. Alloys Compd. **487**, 550 (2009).
[13]C.-J. Liu, A. Bhaskar, and J. J. Yuan, Appl. Phys. Lett. **98**, 214101 (2011).
[14]L. Bocher, M. H. Aguirre, R. Robert, D. Logvinovich, S. Bakardjieva, J. Hejtmanek, and A. Weidenkaff, Acta Mater. **57**, 5667 (2009).
[15]E. Goldyreva, I. Leonidov, M. Patrakeev, and V. Kozhevnikov, J. Solid State Electrochem. **16**, 1187 (2012).
[16]F. Kröger and H. Vink, "Relations between the concentrations of imperfections in crystalline solids," in *Solid State Physics*, edited by F. Seitz and D. Turnbull (Academic Press, 1956), Vol. 3, pp. 307–435.
[17]K. Poeppelmeier, M. Leonowicz, J. Scanlon, J. Longo, and W. Yelon, J. Solid State Chem. **45**, 71 (1982).
[18]Q. He, X. Zhang, H. Hao, and X. Hu, Phys. B **403**, 2867 (2008).
[19]M. Ohtaki, H. Koga, T. Tokunaga, K. Eguchi, and H. Arai, J. Solid State Chem. **120**, 105 (1995).
[20]P. Thiel, J. Eilertsen, S. Populoh, G. Saucke, M. Döbeli, A. Shkabko, L. Sagarna, L. Karvonen, and A. Weidenkaff, J. Appl. Phys. **114**, 243707 (2013).
[21]E. I. Leonidova, I. A. Leonidov, M. V. Patrakeev, and V. L. Kozhevnikov, J. Solid State Electrochem. **15**, 1071 (2011).
[22]P. M. Chaikin and G. Beni, Phys. Rev. B **13**, 647 (1976).
[23]W. Koshibae, K. Tsutsui, and S. Maekawa, Phys. Rev. B **62**, 6869 (2000).
[24]T. D. Sparks, A. Gurlo, and D. R. Clarke, J. Mater. Chem. **22**, 4631 (2012).
[25]J. Briático, B. Alascio, R. Allub, A. Butera, A. Caneiro, M. T. Causa, and M. Tovar, Phys. Rev. B **53**, 14020 (1996).
[26]A. Reller, J. M. Thomas, D. A. Jefferson, and M. K. Uppal, Proc. R. Soc. London, Ser. A **394**, 223 (1984).
[27]S. Mukerjee and J. E. Moore, Appl. Phys. Lett. **90**, 112107 (2007).
[28]D. C. Worledge, L. Miéville, and T. H. Geballe, Phys. Rev. B **57**, 15267 (1998).
[29]S. Ciuchi and S. Fratini, Phys. Rev. B **79**, 035113 (2009).
[30]E. Goldyreva, I. Leonidov, M. Patrakeev, and V. Kozhevnikov, J. Solid State Electrochem. **17**, 1449 (2013).
[31]J. M. De Teresa, K. Dörr, K. H. Müller, L. Schultz, and R. I. Chakalova, Phys. Rev. B **58**, R5928 (1998).
[32]M. E. M. Jorge, M. R. Nunes, R. S. Maria, and D. Sousa, Chem. Mater. **17**, 2069 (2005).
[33]Y. Wang, Y. Sui, H. Fan, X. Wang, Y. Su, W. Su, and X. Liu, Chem. Mater. **21**, 4653 (2009).

[This article is copyrighted as indicated in the article. Reuse of AIP content is subject to the terms at: http://scitation.aip.org/termsconditions. Downloaded to] IP: 129.240.152.45 On: Thu, 13 Mar 2014 16:04:41

6.3 Paper 3

Versatile Apparatus for Thermoelectric Characterisation of Oxides at High Temperatures

M. Schrade, H. Fjeld, T. Norby, T.G. Finstad

submitted to Review of Scientific Instruments

6.4 Paper 4

Oxygen Nonstoichiometry in $(Ca_2CoO_3)_q(CoO_2)$ – A Combined Experimental and Computational Study

M. Schrade, S. Casolo, P. Graham, C. Ulrich, S. Li, O.-M. Løvvik, T.G. Finstad, T. Norby

submitted to the Journal of Physical Chemistry C

7 Further Results and Summarising Discussion

In this chapter, the main findings of the papers will be summarised, discussed and put into a broader context. This also includes further results, which have not been included in the presented papers, but are relevant for the thesis.

7.1 Hall Effect Measurements on $(Ca_2CoO_3)_q\,(CoO_2)$

Hall effect measurements to determine the carrier density are routinely used in standard thermoelectric research to find the optimum doping concentration. We also tried to assess predictions made from the developed defect chemical model on overall charge carrier concentration x and changes in x caused by oxygen vacancies, via the measurement of the Hall coefficent. Again, a single sample was used for all measurements to exclude microstructural and compositional contributions. The sample was equilibrated at high temperatures and under controlled pO_2 and subsequently quenched, providing a constant $\delta \neq 0$ at low temperatures. The room temperature Hall coefficient R_H was measured using a magnetic field of 1.02 T and a maximum current of 1 A. Such high current is needed to measure a statistically significant change of the Hall voltage, when the magnetic field is changed. Influence of a variation of the sample temperature due to Joule heating was minimised by allowing the sample to cool down to room temperature after every single measurement. Each measurement was repeated several times and in random order.

The conductivity and the Hall coefficient of CCO at room temperature are shown in Fig. 7.1. The conductivity decreases, as expected, with increasing δ, comfirming the successful quenching of the sample. The Hall coefficient increases with δ, which indicates a decrease in charge carrier concentration. The values of R_H are in good agreement with values reported for CCO by others (e.g. [81–84]) and similar to those measured on different misfit cobaltites [43]. By using the classical relation $R_H = 1/nq$, where n and q are the concentration and charge of the carriers, respectively, one can in principle relate the Hall coefficient to a carrier concentration. In the present case, the concentration extracted from Hall measurements varies between 4 and $5 \cdot 10^{20}\,\mathrm{cm}^{-3}$, which translates to a molar charge carrier concentration between 0.05 and 0.07. These

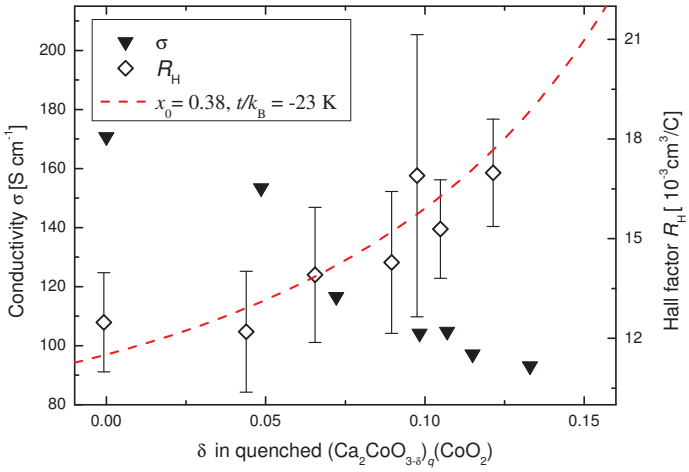

Figure 7.1: Hall measurements of a CCO sample prepared with different oxygen nonstoichiometry δ. The conductivity decreases with increasing δ, while the Hall coefficient increases. For comparison, we show a curve calculated from Eq. (7.1), as explained in the text.

values are much lower than those predicted from the proposed defect chemical model ($0.22 - 0.38$ for the present values of δ).

However, it has been suggested to describe the Hall coefficient in systems based on a triangular lattice, such as the misfit cobaltite family, within a t-J-Hubbard-model [85, 86]:

$$R_H = -\frac{V}{4e}\frac{k_B T}{t}\frac{1+x}{x(1-x)} \tag{7.1}$$

where t is a hopping parameter describing the orbital overlap between neighbouring transition metal sites, V the volume of a unit cell containing one Co_{COL}-atom, and x is the electron concentration with respect to half filling ($\equiv 0$ for $\left[Co^{3+}_{COL}\right] = 0$). Since t is *a priori* unknown, Hall measurements in CCO do not yield the charge carrier concentration directly, despite its general use in the literature. However, if we estimate a value for t/k_B as -23 K – similar to those reported by Hébert *et al.* for other misfit structures [43] – and assume t to be constant with varying δ, we can compare our results with the described model. V is ≈ 80 Å^3 and for the electron concentration x we use a simplified expression, valid at low temperatures, as presented in Manuscript 1: The hole concentration $h(\delta)(\equiv 1 - x)$ of a quenched sample can be expressed as

$$h(\delta) = x_0 - 2 \cdot q \cdot \delta \tag{7.2}$$

where x_0 is the hole concentration of a fully oxidised sample. The resulting curve

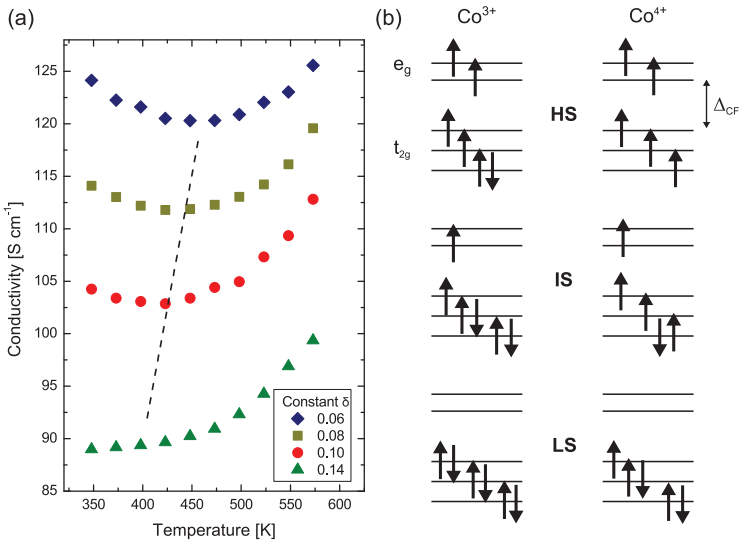

Figure 7.2: (a) The conductivity σ of CCO prepared with different oxygen nonstoichiometry δ at low temperatures. σ undergoes a broad minimum. With increasing δ, σ_{Min} shifts to lower temperatures, indicating a suppression of the transition. (b) Crystal-field splitting Δ_{CF} of the Co:3d-states in an octahedral coordination. The different spin-configurations for both Co^{3+} and Co^{4+} are shown.

from Eq. (7.1) (with $x_0 = 0.38$ as predicted from our defect chemical model) is in good agreement with the experimental R_{H}. We therefore conclude that the carrier concentration in CCO is in fact significantly higher than the values calculated via the classical formula $R_{\mathrm{H}} = 1/nq$. Furthermore, the presented Hall measurements can be used to quantify the parameters t and x_0.

7.2 Metal-Insulator Transition in $(Ca_2CoO_3)_q\,(CoO_2)$

The influence of the oxygen content on the low temperature ($T \leq 300\,\mathrm{K}$) properties of the studied materials was not investigated within the manuscripts in Chapter 6. Still, CCO shows two anomalies in its transport coefficients at temperatures just slightly above room temperature [68,87]. The first one occurs around 380 K and is commonly associated with a spin state transition of the Co^{3+}- and Co^{4+}-ions [81,88,89]. Based on magnetic measurements, it was suggested that at low temperatures, Co^{3+} is in a low spin state ($t_{2g}^6 e_g^0$) and Co^{4+} in an intermediate spin ($t_{2g}^4 e_g^1$) configuration, while – at temperatures above 380 K – it changes to an intermediate ($t_{2g}^5 e_g^1$) and high-spin ($t_{2g}^4 e_g^2$) for the Co^{3+} and Co^{4+}, respectively. This spin state transition is likely to be

accompanied by a transition from a disordered low temperature state to an ordered state at higher temperatures within the rock salt layer [90]. The origin of the second anomaly in the transport properties, manifesting itself in a broad maximum of the resistivity around 490 K, is less clear.

In Fig. 7.2 (a), the in-plane electrical conductivity of a CCO-sample prepared with different values of oxygen nonstoichiometry δ is shown. The temperature corresponding to minimal conductivity for the most oxidised sample agrees well with the one reported by Limelette *et al.* [87]. With increasing concentration of oxygen vacancies δ, we find a shift of the minimum conductivity to lower temperatures. For the most reduced sample ($\delta \approx 0.14$), no minimum in conductivity is found in the investigated temperature range. By the creation of oxygen vacancies, the stress between the two subsystems in CCO is changed, which can alter the crystal field splitting Δ_{CF}. The competing energy scales at play – the Hunds coupling, the crystal field splitting and the bandwidth of the *d*-states – are all comparable [91], making a suppression of the spin state transition by the introduction of oxygen vacancies a plausible scenario.

One should further note that it is not clear whether the spin state transition and the broad conductivity minimum are actually interrelated, as they occur at quite different temperatures. By increasing δ, the hole concentration is reduced, which leads to an increased average distance and thus a higher degree of localisation. This seems to stabilise the insulating/semiconducting state and shift the metal-insulator transition to lower temperatures. A similar behaviour was observed by Nong *et al.* [92]. Therefore, the investigation of the magnetic properties of CCO with different δ, could provide further information on the nature of the spin-state transition and potential long-range ordering.

7.3 Ground State of $(Ca_2CoO_3)_q\,(CoO_2)$

The defect chemical model of CCO developed in Manuscript 1 to describe all charged species is able to reproduce the experimental thermogravimetric results, the extracted thermodynamic parameters were confirmed by the direct measurement of the oxidation enthalpy via TG-DSC, and the proposed relation between the charge carrier concentration and the nonstoichiometry δ ($h = 0.38 - 2q\delta$) can explain the observed Hall coefficient. These findings were used to elucidate the charge transport mechanism of CCO at high temperatures. All experimental results obtained during this thesis can be explained within the presented model, but one has to admit that some results found by other authors and reported in the literature cannot. As mentioned in the introduction, literature addressing the fundamental charge transport properties of CCO is mostly addressing a temperature range below 300 K, making it difficult to directly compare these studies with our results. Yet, observation of significant Co^{2+}

concentrations at room temperature in several publications is puzzling [35,68,93]. On the other hand, no sign of Co^{2+}_{RSL} is found at low temperatures in other studies [19,94].

Co^{2+} in the RSL would increase the concentration of holes (or Co^{4+}) in the COL to balance the overall charge neutrality. The question of a significant Co^{2+} concentration in the RSL is thus equivalent to the one of hole concentration within the COL. The reported values for the hole concentration in CCO vary between 0.3 and 0.6 [19, 20, 87, 94, 95].

We firstly note that the proposed defect chemical model (Eqs. (3.14) and (3.15)) is *not* dependent on the chosen reference state, as long the same defect chemical reactions are considered. It is easy to see that the relevant equations for the equilibrium constants become equivalent to the ones published in Manuscript 1 when chosing e.g. a reference valency of 3.5+ in the COL, resulting in a mixed valent reference state for the cobalt ion in the RSL with an average valence of 2.8+. The physical ground state is defined by the chosen defect chemical equations and not the reference state to denote the considered species.

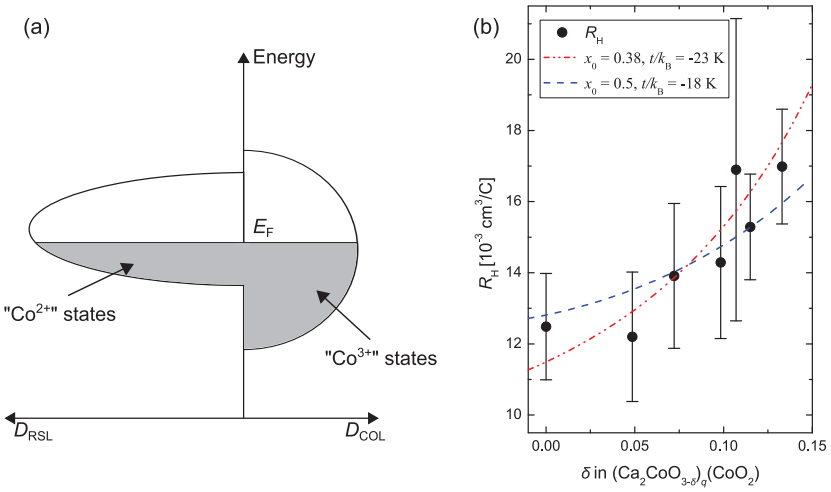

Figure 7.3: (a) Sketch of highest occupied band in CCO, when contributions from the COL and RSL subsystem overlap in energy, resulting in a mixed valent state in *both* subsystems. In the chosen example the average valency in the RSL is 2.8+, and 3.5+ in the COL. (b) Comparison of the experimental Hall coefficient and calculated curves by Eq. (7.1) using different assumptions for the fully oxygenated state of CCO.

On the other hand, the situation is different if we assume a different ground state with a mixed valency in both subsystems as sketched in Fig. 7.3 (a). This state can be constructed from the band diagram sketched in Fig. 3.3 by assuming that the highest

occupied bands of both subsystems overlap in energy. One should keep in mind that this scenario is in disagreement with the detailed study of Takeuchi *et al.* [18]. The electronic states at the Fermi level are now hybridised and have character of both a Co^{2+}_{RSL}- and a Co^{3+}_{COL}-state. As pointed out in Chapter 3, this state – extending spatially across the two subsystems – can in principle still be projected onto its main constituent and then treated by the conventional Kröger-Vink notation for point defects. But to calculate the respective concentrations of both Co^{2+}_{RSL} and Co^{3+}_{COL} species, the relative density of states at the Fermi energy of both subsystems has to be known. The concentration can be expressed as:

$$\left[Co^{2+}_{RSL}\right] = \frac{\int_0^{E_F} D_{RSL}(E)\,\mathrm{d}E}{0.62} \tag{7.3}$$

where D_{RSL} is the partial density of states of the rock salt system and the factor 0.62 reflects the total number of states per formula unit CCO within a rock salt band. The integration has to be performed for the highest (partially) occupied band. The concentration of $\left[Co^{3+}_{COL}\right]$ can be calculated in an analogue way. The Fermi energy E_F is given by solving

$$0.62 = \int_0^{E_F} D_{Tot}(E)\,\mathrm{d}E \tag{7.4}$$

where D_{Tot} is the total density of states of both COL and RSL in the highest occupied band.

From our data, we cannot conclude in favour of one or the other ground state of CCO. But – as illustrated in Fig. 7.3 (b) – the Hall coefficient is sensitive to changes in x_0 and a more detailed and better resolved study of the Hall effect on oxygen deficient samples could provide valuable information.

A possible explanation for the observed concentration of Co^{2+} in CCO by other groups could be due to the presence of excess cobalt, for example on interstitial positions, or (in ceramic samples) as an undetected secondary phase, e.g. CoO or Co_3O_4. Alternatively, the conclusion of $\left[Co^{2+}_{RSL}\right] \neq 0$ from bond length analysis (e.g. [93]), where the interatomic distance is compared to known reference materials, might not hold for a complicated and unusual structure as that of CCO.

7.4 Conclusion: Electronic Properties of $(Ca_2CoO_3)_q\,(CoO_2)$

The misfit calcium cobaltite is the material studied in most detail during this thesis. In this section, the main findings are summarised. A defect chemical model was developed to describe the concentration of charged species in CCO. The misfit structure leads to an inherently defective ground state with a hole concentration of 0.38 per formula unit. At high temperatures and low oxygen partial pressure, CCO can host

a significant concentration of oxygen vacancies within the central Co-O-layer of the rock salt subsystem. In the ground state, cobalt ions within the rock salt layer are in a +3 valence state, but at high temperatures, a significant amount gets thermally excited to +2. A site restriction for the formation of oxygen vacancies was necessary to describe the thermogravimetric data. The oxidation enthalpy of -55 $\mathrm{kJmol^{-1}}$ extracted from this defect chemical model was independently confirmed directly by a measurement via TG-DSC.

Based on these results, the charge transport in CCO at high temperatures was discussed. We concluded that hole-type carriers move itinerantly rather than via localised states. The variation of the Seebeck coefficient with charge carrier concentration and the small observed anisotropy remains puzzling to understand, but we could show that the frequently used Heikes formula cannot be employed for a quantitative analysis in CCO. In general, one can find experimental indication for all predictions drawn from our defect chemical model, and only few publications report on findings which cannot be explained. As shown for the results on quenched samples, the precise control of oxygen content also has a significant influence on the low temperature electronic properties of CCO.

7.5 Thermal Conductivity

In order to determine the theoretical thermoelectric performance of a material via Eq. (1.3), one has to measure also the thermal conductivity κ. Using the laser flash technique, κ is calculated from the measured thermal diffusivity via Eq. (5.3). The specific heat capacity c_p can be measured simultaneously using a reference sample with known c_p. However, as a consequence, the calculated values of κ have a higher inaccurracy as compared to those with an independently determined c_p.

Before presenting the experimental data, we want to give estimates for the electronic contribution to the total thermal conductivity. We have seen in Chapter 2 that the electronic contribution κ_el to the thermal conductivity is related to the conductivity σ via the Lorenz-number L. Although L is not constant and varies with the charge carrier concentration and scattering process, its value does usually not vary by more than a factor of 2 around its textbook value of $L = 2.44 \cdot 10^{-8}\,\mathrm{W\Omega K^{-2}}$. In the case of CMO and CCO, we can therefore estimate κ_el. For CCO, κ_el reaches $0.4\,\mathrm{Wm^{-1}K^{-1}}$ ($\sigma = 100\,\mathrm{Scm^{-1}}$, $T = 900\,^\circ\mathrm{C}$), and for CMO, κ_el is always below $0.2\,\mathrm{Wm^{-1}K^{-1}}$ ($\sigma = 60\,\mathrm{Scm^{-1}}$, $T = 1000\,^\circ\mathrm{C}$). For CCO, one has to further consider the anisotropy of the conductivity in the sample. In single-crystals, the in-plane conductivity σ_ab at room temperature is higher by a factor of ten than the cross-plane σ_c [68], so that the electronic contribution to the total cross-plane thermal conductivity is even lower than calculated from in-plane conductivity data.

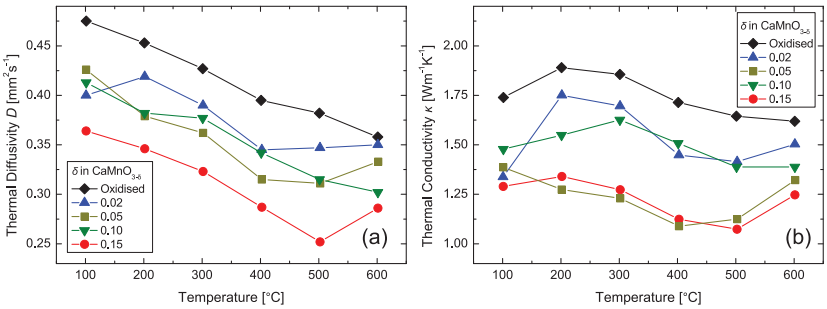

Figure 7.4: (a) Thermal diffusivity D of $CaMnO_{3-\delta}$ prepared with different δ. D is similar for all samples but decreases somewhat with increasing δ. (b) Thermal conductivity κ as calculated from the data in (a) and c_p obtained from a reference sample. No clear trend in κ with varying δ can be observed.

For CMO, the thermal diffusivity and calculated thermal conductivity are shown in Fig. 7.4 for a sample prepared with different oxygen nonstoichiometry δ. The thermal diffusivity seems to decrease somewhat with increasing δ, but no clear trend can be seen in the deduced thermal conductivity. This can be explained by the inaccuracy of determining the specific heat capacity c_p by comparing the maximum temperature rise on the backside of the sample with the one of a reference sample with known c_p.

A similar set of measurements was taken for a sample of CCO and the results are shown in Fig. 7.5. The thermal diffusivity D is practically independent of the oxygen content. However, the calculated thermal conductivity varies for different values of δ, but no clear trend is observed. As neither the relative density, nor the heat capacity are expected to be a sensitive function of δ, we conclude that the variation in Fig. 7.5 (b) is an artefact due to the inaccurate determination of c_p.

As the measured c_p-values are not accurate enough for both CCO and CMO, we limit the discussion of the influence of oxygen nonstoichiometry on the thermal conductivity to the more reliable, directly measured values of the thermal diffusivity.

Point defects like oxygen vacancies might – due to a local change of the mass density – act as a scattering center for phonons, thereby reducing the thermal conductivity and increasing the thermoelectric figure of merit. One can show that the rate for point defect scattering τ_{PD}^{-1} is related to the mass difference between the mass of the point defect, m_i, with the concentration x_i, and the average atomic mass in the structure $\overline{m}$ [96]:

$$\tau_{PD}^{-1} \propto \sum_i x_i \left(\frac{m_i - \overline{m}}{\overline{m}} \right)^2 \tag{7.5}$$

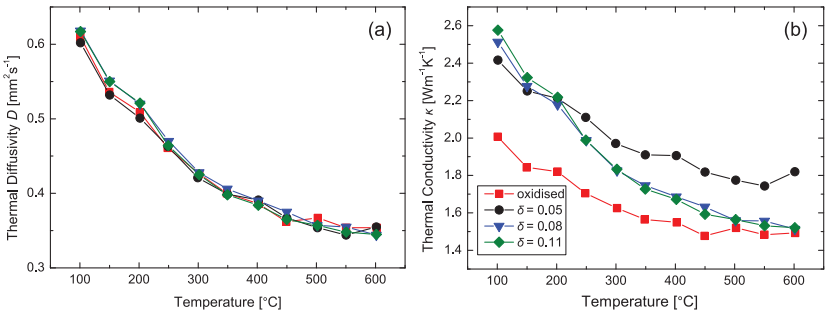

Figure 7.5: (a) Thermal diffusivity D of $(Ca_2CoO_{3-\delta})_q(CoO_2)$ prepared with different δ. No variation of D is observed when δ is varied. (b) Thermal conductivity κ as calculated from the data in (a) and c_p obtained from a reference sample. The observed difference in κ is discussed as an artefact in the text.

An analogue expression can be found for CCO. We can then estimate the influence of point defects on the thermal conductivity of both CMO and CCO. The scattering by variations in the mass density as a function of oxygen nonstoichiometry δ can be written for CMO as:

$$\tau_{PD}^{-1} \propto \frac{1}{5}\left(\frac{m_{Ca}-\overline{m}}{\overline{m}}\right)^2 + \frac{1}{5}\left(\frac{m_{Mn}-\overline{m}}{\overline{m}}\right)^2 + \frac{3-\delta}{5}\left(\frac{m_{O}-\overline{m}}{\overline{m}}\right)^2 + \frac{\delta}{5}\left(\frac{m_{V_O^{\bullet\bullet}}-\overline{m}}{\overline{m}}\right)^2 \tag{7.6}$$

Calculating the relative change $\Gamma(\delta) = 1 - \tau_{PD}^{-1}(\delta)/\tau_{PD}^{-1}(0)$ for both CMO and CCO, one obtains $\Gamma_{CMO}(0.15) \approx 0.04$ and $\Gamma_{CCO}(0.15) \approx 0.015$. The relative change of τ_{PD}^{-1} in CMO is thus 2.5 times larger than that in CCO for the same oxygen vacancy concentration δ. However, the calculated relative decrease is much lower than the observed variation of $\approx 20\,\%$ for CMO (Fig. 7.4 (a)). Still, we can rationalise the observation that we do see changes in the thermal diffusivity of CMO when the concentration of oxygen vacancies is changed, but that the analogue variation in CCO is too small to be experimentally resolved.

7.6 zT of $(Ca_2CoO_3)_q\,(CoO_2)$

Now, after we presented all the relevant experimental data, we can calculate the influence of oxygen vacancies on the thermoelectric figure of merit. The anisotropy of the transport properties for a ceramic sample has to be considered carefully: We have measured the electrical conductivity perpendicular to the compacting direction, that is, mostly parallel to the *ab*-plane of CCO-crystallites. The Seebeck coefficient and the thermal conductivity have been measured cross-plane, i.e. along the *c*-axis.

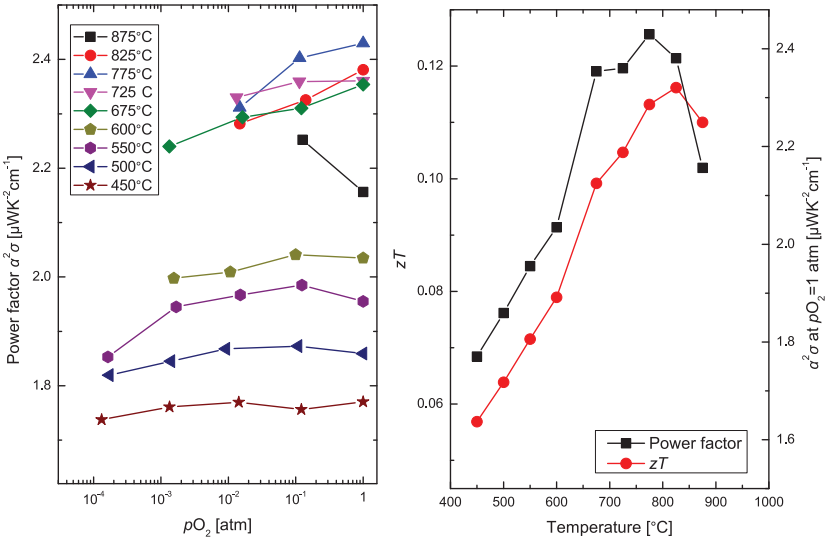

Figure 7.6: (a) The in-plane power factor $\alpha^2\sigma$ of CCO as a function of pO_2 and temperature T, calculated assuming that the Seebeck coefficient in CCO is isotropic as suggested in Manuscript 3. $\alpha^2\sigma$ increases somewhat with T but it appears to be rather independent of pO_2. (b) $\alpha^2\sigma$ at $pO_2 = 1\,\text{atm}$ as a function of T. The in-plane thermoelectric figure of merit zT is calculated using a temperature independent thermal conductivity $\kappa = 2.25\,\text{Wm}^{-1}\text{K}^{-1}$, as explained in the text.

In Manuscript 3 we find that the anisotropy of the Seebeck coefficient is only minor, if existent at all. We can thus use the measured cross-plane Seebeck coefficient to estimate the in-plane zT. In Fig. 7.6 (a) we plot the power factor $\alpha^2\sigma$ as a function of pO_2 and temperature, calculated from the data presented in Manuscript 1. $\alpha^2\sigma$ increases with temperature, but is almost independent of pO_2 or, equivalently, of the concentration of oxygen vacancies. The power factor reaches values around $2.4\,\mu\text{WK}^{-2}\text{cm}^{-1}$.

Furthermore, Saucke *et al.* recently reported on the anisotropy of the thermal diffusivity D in ceramic CCO samples and found $D_{ab}/D_c \approx 1.5$ in the whole temperature range [83]. From this result, we are able to estimate the in-plane thermal conductivity of CCO: The calculated cross-plane thermal conductivity of CCO in Fig. 7.5 (b) seems to converge at $1.5\,\text{Wm}^{-1}\text{K}^{-1}$ at elevated temperatures. Using this value, we estimate $\kappa_{\text{in-plane}} = 2.25\,\text{Wm}^{-1}\text{K}^{-1}$. Combining all results, the thermoelectric figure of merit zT can be calculated to be in the order of 0.1.

One should note that the studied sample only had a relative density of $\approx 80\,\%$, allowing relatively short equilibration times, but limiting the electrical conductivity

due to increased scattering at the grain boundaries. The Seebeck coefficient is less dependent on the microstructural characteristics of the sample. Thus, a dense sample shows a significantly higher conductivy compared to a porous one, while retaining similar values of the Seebeck coefficient (c.f. the sample used for the quenching experiments in Manuscript 1). This sample showed a conductivity of $\approx 180\,\mathrm{Scm}^{-1}$ at high temperatures, almost twice the value of the porous sample, while the Seebeck coefficient was in the same order (around $150\,\mu\mathrm{VK}^{-1}$). In this case, the power factor is $4\,\mu\mathrm{WK}^{-2}\mathrm{cm}^{-1}$, comparable with the best values reported in the literature for undoped CCO [39, 97–101]. Assuming identical values of κ, the zT of dense CCO ceramics is then estimated to be around 0.2 at temperatures between 600 and 900 °C. The tuning of the charge carrier concentration by aliovalent doping may improve this value. However, one has to keep in mind that CCO is already *intrinsically* doped to a high degree (corresponding to a molar charge carrier concentration x of 0.38, as shown in Manuscript 1) due to its misfit structure. Therefore, typical dopant concentrations will only lead to relatively minor changes in x, limiting the potential increase in zT.

However, some authors rationalise the (unexpected) increase in conductivity by donor doping of the material (e.g. La^{3+} or Bi^{3+} for Ca^{2+}) by a variation of the carrier mobility. They argue that a variation of the internal stress between the two subsystems is overcompensating the decrease in carrier concentration (e.g. [101–103]). Yet, there are also contradicting reports on the regular decrease of the conductivity when CCO is doped with the same donor species [39, 104]. In this light – combined with our findings of the sensitivity of σ on the relative density of the ceramic samples – the observed increase of mobility found in some donor doped samples may be rather a microstructural effect than related to internal stress inside the crystallites.

This conclusion is supported by our findings in Manuscript 1. We could see that the calculated carrier mobility seems to be rather independent of the oxygen vacancy concentration, although it is reasonable to expect a variation of the internal stress when oxygen vacancies are formed. However, one may speculate that – as oxygen vacancies are only formed within the central rock salt layer – the induced stress is already released inside the rock salt subsystem and the conducting COL remains unaffected. On the other hand, doping on the Ca-site (located on the outer rock salt layer) could then influence the hole propagation within the COL and explain the unexpected doping behaviour.

In any case, considering the number of different attempts already reported, it is unlikely to expect a dramatic increase of the power factor of CCO.

Finally, the thermal conductivity cannot be reduced below a certain, amorphous limit. Cahill *et al.* derived an expression for the minimum conductivity of an disor-

dered crystal [105]:

$$\kappa_{\mathrm{Min}} = \left(\frac{\pi}{6}\right)^{1/3} \mathrm{k_B}\, n^{2/3} v \left(\frac{T}{\theta}\right)^2 \int_0^{\theta/T} \frac{x^3 e^x}{(e^x-1)^2}\,\mathrm{d}x \tag{7.7}$$

where n is the number of atoms per unit volume, v the sound velocity, and θ the Debye temperature. Using reported approximate values of $v = 4000\,\mathrm{ms^{-1}}$ and $\theta = 600\,\mathrm{K}$[1], we can estimate $\kappa_{\mathrm{Min}} \approx 0.5\,\mathrm{Wm^{-1}s^{-1}}$ [106, 107]. So, even when assuming that a hypothetical reduction of the thermal conductivity in CCO to the amorphous limit could be achieved, that it does not pertubate the electronic properties, and that it could be sustained during long-term high temperature application, a twofold increase in zT due to a reduction of κ may be the maximum, even under these very optimistic premises.

In summary, evaluating all available data realistically, it can be concluded that the (reproducible) zT of polycrystalline CCO might be limited to values well below 0.5.

7.7 $CaMnO_{3-\delta}$

In Manuscript 2, we explained the unusual simultaneous decrease of the absolute Seebeck coefficient and electrical conductivity upon oxygen vacancy formation as the indication of strongly interacting small polarons being the charge carrier in $CaMnO_{3-\delta}$. Can this model also explain the reported conductivity data in $CaMnO_3$-based, aliovalently doped compounds?

In calcium manganite doped on the *A*-site with La, Y, and Ce, the maximum conductivity was found at a doping level x of 0.12 (for La and Y) and 0.06 (for Ce), both at room temperature and at 1000 K [108]. The authors interpret this behaviour as the signature of charge ordered clusters which form when the carrier concentration exceeds a certain value. While this scenario may well be a plausible explanation at room temperature, (short-range) charge ordering is unlikely to persist up to the temperatures investigated by Wang *et al.* and in our study. Furthermore, the authors did not discuss the significant contribution of intrinsic, thermally excited carriers at high temperatures. On the other hand, the model proposed in Manuscript 2 includes a shift of the charge carrier concentration at maximum conductivity with temperature:

$$\sigma(x) \propto x \cdot \exp\left(-\frac{E_\xi \cdot x}{\mathrm{k_B}T}\right) \;\rightarrow\; x(\sigma_{\mathrm{Max}}) = \frac{\mathrm{k_B}T}{E_\xi} \tag{7.8}$$

The model can thus conveniently explain the behaviour observed by Wang *et al.*.

We note that also another discussed origin of the unusual doping dependency in

[1] In fact, both θ and v are dependent on the crystal direction. The reported values are a crude average for a polycrystalline sample, but help to give a rough estimate for κ_{Min}.

CMO – the variation of the Mn-O-Mn-bond angle with varying doping levels [109] – can be excluded at the high temperature and low pO_2 studied in Manuscript 2, as the structure was found to be cubic across the whole experimental range [110].

A different situation, where the proposed model for charge transport in $CaMnO_{3-\delta}$ is not valid, may be found, though, when $CaMnO_3$ is doped on the *B*-site. Recently, *B*-site doping with tungsten was discussed to lead to itinerant conduction within an impurity band [52].

Finally, we want to estimate the potential zT of ceramic samples based on $CaMnO_3$. At the highest temperatures ($T \approx 1000\,^{\circ}C$), oxygen vacancies become the dominating defect and the power factor is around $1.8\,\mu WK^{-2}cm^{-1}$, effectively independent of the extrinsic doping level (e.g. [53]). Combined with an optimistic guess for the optimised thermal conductivity $\kappa \approx 1\,Wm^{-1}K^{-1}$, this results in $zT \approx 0.22$ at $1000\,^{\circ}C$. At lower temperatures, somewhat higher power factors are reported (e.g. $2.4\,\mu WK^{-2}cm^{-1}$ [89] or $3.3\,\mu WK^{-2}cm^{-1}$ [104], both obtained at $600\,^{\circ}C$). Assuming identical values for κ, zT can be estimated to be in the order of 0.3. As discussed in Manuscript 2, the strong mutual repulsion of charge carriers in $CaMnO_3$ limits the power factor and therefore an increase of zT beyond this value.

7.8 Outlook

This thesis investigated the influence of oxygen nonstoichiometry on the thermoelectric properties of $(Ca_2CoO_3)_q(CoO_2)$ and $CaMnO_3$. Since a single sample is used, *in situ* changes of the carrier concentration via a controlled variation of the oxygen content, allow the investigation of the transport properties without consideration of microstructural effects. The obtained results elucidate the charge transport mechanism in the studied materials and help to understand the high temperature thermoelectric performance of related oxides.

Many interesting questions around the studied materials remain open. For example, a structural investigation of CCO at high temperatures and controlled pO_2 could elucidate the influence of internal stress and structural variations in the rock salt subsystem on the transport parameters in CCO, as speculated in Manuscript 4. Studying the oxygen nonstoichiometry of a misfit compound without mixed-valent species inside the rock salt layer (e.g. $(Bi_2Ca_2O_4)_q(CoO_2)$) would presumably result in a simpler defect chemistry, as all formed oxygen vacancies may be compensated by Co^{3+} in the CoO_2 layer. Furthermore, a variation of the oxygen nonstoichiometry is expected to also vary the electronic and magnetic properties of the studied materials at low temperatures – as indicated in Fig. 7.2 – but systematic studies have not been carried out yet.

These questions address the fundamental properties of the materials under study,

thereby following the main lines of this thesis. However, I want to conclude this thesis by pointing out some prospects of oxides for thermoelectric energy harvesting applications. When implementing the p- and n- materials of choice into a thermoelectric generator, one central problem is to reduce the contact resistance of the two materials. In laboratory-scale demonstration modules based on oxide materials, contacting is usually done using a paste with a high noble metal content (see [111] for an overview over all-oxide TE modules). However, this complicates device fabrication and increases the module cost, so that simpler and cheaper contacting concepts need to be developed.

In any case, the zT values of the oxide materials studied today will not reach the values of state-of-the-art thermoelectric materials. Still, it has been argued that thermoelectric energy conversion, despite its low efficiency, is economically sustainable in some applications, if the lifetime of the modules can be increased to several years [112]. This stability requirement imposes several challenges on the (oxide) materials used in a generator designed for high temperature applications. The module is exposed to both thermal and mechanical stress, due to thermal expansion, large temperature gradients, and temperature cycling. Long-term stability is further impaired by possible interdiffusion and reaction of the p- and n- material at the hot side of the module. When aiming at optimum long-term module performance, these challenges call for the simultaneous investigation of a p-n-pair, rather than optimising a single material, with no compatible counterpart available.

Bibliography

[1] Goldsmid, J. (2009) Introduction to Thermoelectricity, Springer, Berlin, .

[2] Snyder, G. J. and Toberer, E. S. (2008) *Nature Materials* **7**, 105–114.

[3] Vining, C. (2009) *Nature Materials* **8**, 83–85.

[4] Terasaki, I., Sasago, Y., and Uchinokura, K. (1997) *Phys. Rev. B* **56(20)**, R12685–R12687.

[5] Emin, D. Wiley Encyclopedia of Electrical and Electronics Engineering chapter Seebeck Effect, pp. 1–29 John Wiley & Sons, Inc. (1999).

[6] MacDonald, D. (2006) Thermoelectricity - An Introduction to the Principles, Dover publications, New York, .

[7] Wilson, A. (1958) The Theory of Metals, The Syndics of the Cambridge University Press, .

[8] Ziman, J. (1972) Principles of the Theory of Solids, Cambridge University Press, .

[9] Mott, N. and Jones, H. (1958) The Theory of the Properties of Metals and Alloys, Dover publications, New York, .

[10] Cutler, M., Leavy, J. F., and Fitzpatrick, R. L. (1964) *Phys. Rev.* **133(4A)**, A1143–A1152.

[11] Hubbard, J. (1963) *Proceedings of the Royal Society of London. Series A. Mathematical and Physical Sciences* **276(1365)**, 238–257.

[12] Fazekas, P. (1999) Lecture Notes on Electron Correlation and Magnetism, World Scientific, Singapore, .

[13] Dudarev, S. L., Botton, G. A., Savrasov, S. Y., Humphreys, C. J., and Sutton, A. P. (1998) *Phys. Rev. B* **57**, 1505–1509.

[14] Anisimov, V. I., Aryasetiawan, F., and Lichtenstein, A. I. (1997) *Journal of Physics: Condensed Matter* **9(4)**, 767.

[15] Kröger, F. and Vink, H. Relations between the Concentrations of Imperfections in Crystalline Solids p. 307–435 Academic Press (1956).

[16] Inoue, T., Seki, N., Kamimae, J.-I., Eguchi, K., and Arai, H. (1991) *Solid State Ionics* **48(3–4)**, 283 – 288.

[17] Choi, G. M. and Tuller, H. L. (1988) *Journal of the American Ceramic Society* **71(4)**, 201–205.

[18] Takeuchi, T., Kondo, T., Takami, T., Takahashi, H., Ikuta, H., Mizutani, U., Soda, K., Funahashi, R., Shikano, M., Mikami, M., Tsuda, S., Yokoya, T., Shin, S., and Muro, T. (2004) *Phys. Rev. B* **69(12)**, 125410.

[19] Yang, G., Ramasse, Q., and Klie, R. F. (2008) *Phys. Rev. B* **78**, 153109.

[20] Rébola, A., Klie, R., Zapol, P., and Öğüt, S. (2012) *Phys. Rev. B* **85**, 155132.

[21] Hébert, S. and Maignan, A. Thermoelectric Oxides pp. 203–255 John Wiley & Sons, Ltd (2010).

[22] Fergus, J. W. (2012) *Journal of the European Ceramic Society* **32(3)**, 525 – 540.

[23] Foo, M. L., Wang, Y., Watauchi, S., Zandbergen, H. W., He, T., Cava, R. J., and Ong, N. P. (2004) *Phys. Rev. Lett.* **92**, 247001.

[24] Takada, K., Sakurai, H., Takayama-Muromachi, E., Izumi, F., Dilanian, R., and Sasaki, T. (2003) *Nature* **422**, 53–55.

[25] Koshibae, W., Tsutsui, K., and Maekawa, S. (2000) *Phys. Rev. B* **62(11)**, 6869–6872.

[26] Wang, Y., Rogado, N. S., Cava, R. J., and Ong, N. P. (2003) *Nature* **423**, 425–428.

[27] Singh, D. J. (2000) *Phys. Rev. B* **61**, 13397–13402.

[28] Tsai, P. H., Norby, T., Tan, T. T., Donelson, R., Chen, Z. D., and Li, S. (2010) *Applied Physics Letters* **96(14)**, 141905.

[29] Stoklosa, A., Molenda, J., and Than, D. (1985) *Solid State Ionics* **15(3)**, 211 – 216.

[30] Bañobre-López, M., Rivadulla, F., Caudillo, R., López-Quintela, M. A., Rivas, J., and Goodenough, J. B. (2005) *Chemistry of Materials* **17(8)**, 1965–1968.

[31] Karppinen, M., Asako, I., Motohashi, T., and Yamauchi, H. (2005) *Phys. Rev. B* **71**, 092105.

[32] Vengust, D., Jancar, B., Sestan, A., Ponikvar Svet, M., Budic, B., and Suvorov, D. (2013) *Chemistry of Materials* **25(23)**, 4791–4797.

[33] Casolo, S., Løvvik, O. M., Fjeld, H., and Norby, T. (2012) *Journal of Physics: Condensed Matter* **24(47)**, 475505.

[34] Miyazaki, Y., Onoda, M., Oku, T., Kikuchi, M., Ishii, Y., Ono, Y., Morii, Y., and Kajitani, T. (2002) *Journal of the Physical Society of Japan* **71(2)**, 491–497.

[35] Muguerra, H., Grebille, D., and Bourée, F. Apr 2008 *Acta Crystallographica Section B* **64(2)**, 144–153.

[36] Grebille, D., Lambert, S., Bourée, F., and Petříček, V. Oct 2004 *Journal of Applied Crystallography* **37(5)**, 823–831.

[37] Karppinen, M., Fjellvåg, H., Konno, T., Morita, Y., Motohashi, T., and Yamauchi, H. (2004) *Chemistry of Materials* **16(14)**, 2790–2793.

[38] Shimoyama, J.-I., Horii, S., Otzschi, K., Sano, M., and Kishio, K. (2003) *Japanese Journal of Applied Physics* **42(Part 2, No. 2B)**, L194–L197.

[39] Moser, D., Karvonen, L., Populoh, S., Trottmann, M., and Weidenkaff, A. (2011) *Solid State Sciences* **13(12)**, 2160 – 2164.

[40] Ling, C. D., Aivazian, K., Schmid, S., and Jensen, P. (2007) *Journal of Solid State Chemistry* **180(4)**, 1446 – 1455.

[41] Leligny, H., Grebille, D., Pérez, O., Masset, A.-C., Herveieu, M., Michel, C., and Raveau, B. (1999) *Comptes Rendus de l'Académie des Sciences - Series {IIC} - Chemistry* **2(7–8)**, 409 – 414.

[42] Itoh, T. and Terasaki, I. (2000) *Japanese Journal of Applied Physics* **39(Part 1, No. 12A)**, 6658–6660.

[43] Hébert, S., Kobayashi, W., Muguerra, H., Bréard, Y., Raghavendra, N., Gascoin, F., Guilmeau, E., and Maignan, A. (2013) *physica status solidi (a)* **210(1)**, 69–81.

[44] Hayashi, K., Nozaki, T., and Kajitani, T. (2007) *Japanese Journal of Applied Physics* **46(8A)**, 5226–5229.

[45] Maignan, A., Eyert, V., Martin, C., Kremer, S., Frésard, R., and Pelloquin, D. (2009) *Phys. Rev. B* **80**, 115103.

[46] Maignan, A., Martin, C., Frésard, R., Eyert, V., Guilmeau, E., Hébert, S., Poienar, M., and Pelloquin, D. (2009) *Solid State Communications* **149(23–24)**, 962–967.

[47] Tate, J., Jayaraj, M., Draeseke, A., Ulbrich, T., Sleight, A., Vanaja, K., Nagarajan, R., Wager, J., and Hoffman, R. (2002) *Thin Solid Films* **411(1)**, 119 – 124.

[48] Maignan, A., Caignaert, V., Raveau, B., Khomskii, D., and Sawatzky, G. (2004) *Phys. Rev. Lett.* **93**, 026401.

[49] Bocher, L., Aguirre, M. H., Logvinovich, D., Shkabko, A., Robert, R., Trottmann, M., and Weidenkaff, A. (2008) *Inorganic Chemistry* **47(18)**, 8077–8085.

[50] Bakken, E., Norby, T., and Stølen, S. (2005) *Solid State Ionics* **176(1–2)**, 217–223.

[51] Goldyreva, E., Leonidov, I., Patrakeev, M., and Kozhevnikov, V. (2012) *Journal of Solid State Electrochemistry* **16**, 1187–1191.

[52] Thiel, P., Eilertsen, J., Populoh, S., Saucke, G., Döbeli, M., Shkabko, A., Sagarna, L., Karvonen, L., and Weidenkaff, A. (2013) *Journal of Applied Physics* **114(24)**, 243707.

[53] Bocher, L., Aguirre, M. H., Robert, R., Logvinovich, D., Bakardjieva, S., Hejtmanek, J., and Weidenkaff, A. (2009) *Acta Materialia* **57(19)**, 5667 – 5680.

[54] Uchida, K., Tsuneyuki, S., and Schimizu, T. (2003) *Phys. Rev. B* **68**, 174107.

[55] Okuda, T., Nakanishi, K., Miyasaka, S., and Tokura, Y. (2001) *Phys. Rev. B* **63**, 113104.

[56] Koumoto, K., Wang, Y., Zhang, R., Kosuga, A., and Funahashi, R. (2010) *Annual Review of Materials Research* **40(1)**, 363–394.

[57] Chan, N. H., Sharma, R. K., and Smyth, D. M. (1981) *Journal of The Electrochemical Society* **128(8)**, 1762–1769.

[58] Sagarna, L., Shkabko, A., Populoh, S., Karvonen, L., and Weidenkaff, A. (2012) *Applied Physics Letters* **101(3)**, 033908.

[59] Ohtaki, M., Tsubota, T., Eguchi, K., and Arai, H. (1996) *Journal of Applied Physics* **79(3)**, 1816–1818.

[60] Ohtaki, M., Araki, K., and Yamamoto, K. (2009) *Journal of Electronic Materials* **38(7)**, 1234–1238.

[61] Lany, S. and Zunger, A. (2007) *Phys. Rev. Lett.* **98**, 045501.

[62] Bérardan, D., Byl, C., and Dragoe, N. (2010) *Journal of the American Ceramic Society* **93(8)**, 2352–2358.

[63] Vogel-Schäuble, N., Dujardin, R., Weidenkaff, A., and Aguirre, M. (2012) *Journal of Electronic Materials* **41(6)**, 1606–1614.

[64] Bérardan, D., Guilmeau, E., Maignan, A., and Raveau, B. (2008) *Solid State Communications* **146(1–2)**, 97 – 101.

[65] Ohya, Y., Yamamoto, T., and Ban, T. (2008) *Journal of the American Ceramic Society* **91(1)**, 240–245.

[66] Wit, J. D., Unen, G. V., and Lahey, M. (1977) *Journal of Physics and Chemistry of Solids* **38(8)**, 819 – 824.

[67] González, G. B., Mason, T. O., Quintana, J. P., Warschkow, O., Ellis, D. E., Hwang, J.-H., Hodges, J. P., and Jorgensen, J. D. (2004) *Journal of Applied Physics* **96(7)**, 3912–3920.

[68] Masset, A. C., Michel, C., Maignan, A., Hervieu, M., Toulemonde, O., Studer, F., Raveau, B., and Hejtmanek, J. (2000) *Phys. Rev. B* **62**, 166–175.

[69] Kraus, W. and Nolze, G. Powdercell 2.4 for windows (1999).

[70] Sedmidubský, D., Jakeš, V., Jankovský, O., Leitner, J., Sofer, Z., and Hejtmánek, J. (2012) *Journal of Solid State Chemistry* **194(0)**, 199 – 205.

[71] Wakisaka, Y., Hirata, S., Mizokawa, T., Suzuki, Y., Miyazaki, Y., and Kajitani, T. (2008) *Phys. Rev. B* **78**, 235107.

[72] Tang, G., Xu, F., Zhang, D., and Wang, Z. (2013) *Ceramics International* **39(2)**, 1341 – 1344.

[73] Huang, Y., Zhao, B., Ang, R., Lin, S., Huang, Z., Tan, S., Liu, Y., Song, W., and Sun, Y. (2013) *The Journal of Physical Chemistry C* **117(22)**, 11459–11470.

[74] Biesinger, M. C., Payne, B. P., Grosvenor, A. P., Lau, L. W., Gerson, A. R., and Smart, R. S. (2011) *Applied Surface Science* **257(7)**, 2717 – 2730.

[75] Parker, W. J., Jenkins, R. J., Butler, C. P., and Abbott, G. L. (1961) *Journal of Applied Physics* **32(9)**, 1679–1684.

[76] Salmon, D. and Tye, R. (2010) *International Journal of Thermophysics* **31(2)**, 338–354.

[77] Kjølseth, C., Wang, L.-Y., Haugsrud, R., and Norby, T. (2010) *Solid State Ionics* **181(39–40)**, 1740 – 1745.

[78] Suresh, A., Mayo, M. J., and Porter, W. D. 12 2003 *Journal of Materials Research* **18**, 2912–2921.

[79] Eysel, W. and Breuer, K.-H. Analytical Calorimetry chapter Differential Scanning Calorimetry: Simultaneous Temperature and Calorimetric Calibration, pp. 67–80 Plenum Publishing Corp. (1984).

[80] Breuer, K.-H. and Eysel, W. (1982) *Thermochimica Acta* **57(3)**, 317 – 329.

[81] Wu, T., Tyson, T. A., Bai, J., Pandya, K., Jaye, C., and Fischer, D. (2013) *J. Mater. Chem. C* **1**, 4114–4121.

[82] Wang, Y., Sui, Y., Cheng, J., Wang, X., Su, W., Liu, X., and Fan, H. J. (2010) *The Journal of Physical Chemistry C* **114(11)**, 5174–5181.

[83] Saucke, G., Populoh, S., Vogel-Schäuble, N., Sagarna, L., Mogare, K., Karvonen, L., and Weidenkaff, A. 1 2013 *MRS Online Proceedings Library* **1543**, 83–92.

[84] Xu, L., Li, F., and Wang, Y. (2010) *Journal of Alloys and Compounds* **501(1)**, 115 – 119.

[85] Kumar, B. and Shastry, B. S. (2003) *Phys. Rev. B* **68**, 104508.

[86] Kumar, B. and Sriram Shastry, B. Feb 2004 *Phys. Rev. B* **69**, 059901.

[87] Limelette, P., Hardy, V., Auban-Senzier, P., Jérome, D., Flahaut, D., Hébert, S., Frésard, R., Simon, C., Noudem, J., and Maignan, A. (2005) *Phys. Rev. B* **71**, 233108.

[88] Sugiyama, J., Xia, C., and Tani, T. (2003) *Phys. Rev. B* **67**, 104410.

[89] Yang, G., Ramasse, Q., and Klie, R. F. (2009) *Applied Physics Letters* **94(9)**, 093112.

[90] Muguerra, H. and Grebille, D. Dec 2008 *Acta Crystallographica Section B* **64(6)**, 676–683.

[91] Raveau, B. and Seikh, M. M. Crystal Chemistry of Cobalt Oxides pp. 3–70 Wiley-VCH Verlag GmbH & Co. KGaA (2012).

[92] Van Nong, N., Pryds, N., Linderoth, S., and Ohtaki, M. (2011) *Advanced Materials* **23(21)**, 2484–2490.

[93] Lambert, S., Leligny, H., and Grebille, D. (2001) *Journal of Solid State Chemistry* **160(2)**, 322 – 331.

[94] Mizokawa, T., Tjeng, L. H., Lin, H.-J., Chen, C. T., Kitawaki, R., Terasaki, I., Lambert, S., and Michel, C. May 2005 *Phys. Rev. B* **71**, 193107.

[95] Eng, H. W., Limelette, P., Prellier, W., Simon, C., and Frésard, R. Jan 2006 *Phys. Rev. B* **73**, 033403.

[96] Terry M. Tritt, (ed.) (2004) Thermal Conductivity - Theory, Properties, and Applications, Kluwer Academic / Plenum Publishers, .

[97] Lin, Y.-H., Lan, J., Shen, Z., Liu, Y., Nan, C.-W., and Li, J.-F. (2009) *Applied physics letters* **94(7)**, 072107.

[98] Liu, H., Song, Y., Zhang, S., Zhao, X., and Wang, F. (2009) *Journal of Physics and Chemistry of Solids* **70(3–4)**, 600 – 603.

[99] Mikami, M., Guilmeau, E., Funahashi, R., Chong, K., and Chateigner, D. (2005) *Journal of Materials Research* **20**, 2491–2497.

[100] Tian, R., Donelson, R., Ling, C. D., Blanchard, P. E. R., Zhang, T., Chu, D., Tan, T. T., and Li, S. (2013) *The Journal of Physical Chemistry C* **117(26)**, 13382–13387.

[101] Xu, G., Funahashi, R., Shikano, M., Matsubara, I., and Zhou, Y. (2002) *Applied Physics Letters* **80(20)**, 3760–3762.

[102] Matsubara, I., Funahashi, R., Shikano, M., Sasaki, K., and Enomoto, H. (2002) *Applied Physics Letters* **80(25)**, 4729–4731.

[103] Lin, Y.-H., Nan, C.-W., Liu, Y., Li, J., Mizokawa, T., and Shen, Z. (2007) *Journal of the American Ceramic Society* **90(1)**, 132–136.

[104] Zhang, F., Lu, Q., Li, T., Zhang, X., Zhang, J., and Song, X. (2013) *Journal of Rare Earths* **31(8)**, 778 – 783.

[105] Cahill, D. G., Watson, S. K., and Pohl, R. O. Sep 1992 *Phys. Rev. B* **46**, 6131–6140.

[106] Altin, S., Bayri, A., Demirel, S., and Aksan, M. (2014) *Current Applied Physics*.

[107] Wang, Y., Sui, Y., Cheng, J., Wang, X., and Su, W. (2007) *Journal of Physics: Condensed Matter* **19(35)**, 356216.

[108] Wang, Y., Sui, Y., Wang, X., and Su, W. (2009) *Journal of Physics D: Applied Physics* **42(5)**, 055010.

[109] Flahaut, D., Mihara, T., Funahashi, R., Nabeshima, N., Lee, K., Ohta, H., and Koumoto, K. (2006) *Journal of Applied Physics* **100(8)**, 084911.

[110] Leonidova, E. I., Leonidov, I. A., Patrakeev, M. V., and Kozhevnikov, V. L. (2011) *Journal of Solid State Electrochemistry* **15**, 1071–1075.

[111] Van, N. N. and Pryds, N. (2013) *Advances in Natural Sciences: Nanoscience and Nanotechnology* **4(2)**, 023002.

[112] Narducci, D. (2011) *Applied Physics Letters* **99(10)**, 102104.